

**DEVELOPMENT OF A NEW ANTISCALANT FOR
MINIMIZATION OF STIBNITE SCALING IN
GEOHERMAL BINARY PLANTS**

**A Thesis Submitted to
the Graduate School of Engineering and Sciences of
İzmir Institute of Technology
in Partial Fulfillment of the Requirements for the Degree of**

MASTER OF SCIENCE

in Materials Science and Engineering

**by
Emre KARABURUN**

**March 2021
İZMİR**

ACKNOWLEDGEMENTS

First of all, I would like to thank my advisor Prof. Mustafa M. DEMİR, for his guidance and assistance throughout my master's. He always approaches me as a friend and shared his knowledge to improve myself very well.

Also I would like to thank my co-advisor Prof. Dr. Alper BABA, for his precious comments and thoughts for my thesis. Moreover, I would like to thank the committee members of this thesis; Prof. Dr. Mehmet İrfan YEŞİLNACAR for taking his precious time for me and his valuable comments and Assoc. Prof. Dr. Yaşar AKDOĞAN for his guidance.

I would also like to thank the member of Demir Research Group; Tuğçe Aybüke Arıca GÜVENÇ, Hürriyet YÜCE, Anılcan KUŞ and Celal ÇİFTÇİ for their supports during my master and special thanks to Gökhan TOPÇU for his brotherhood and mentorship.

In addition, I would like to thank to Ezgi VURAL, Beraat Umur KAYA, Suay Dartar, Yankı Öncü Yayak, and Alper ŞAHİN for their friendship and continual support.

Finally, special thanks to my love Bengisu KANTEKİN for her support during my MSc life. When my mood was bad, she was always by my side and encouraged me to do my best. Thanks to her I never give up.

We thank EU for the PROJECT entitled REFLECT: “Redifining geothermal fluid properties at extreme conditions to optimize future geothermal energy extraction” Grant Agreement No. 850626.

ABSTRACT

DEVELOPMENT OF A NEW ANTISCALANT FOR MINIMIZATION OF STIBNITE SCALING IN GEOTHERMAL BINARY PLANTS

Demand for renewable and sustainable energy resources has been increasing in recent years due to the adverse effects of fossil energy resources (gases, oil, coal ect,) on human health and nature. Since geology properties of our country is rich in geothermal energy resources, there is a remarkable increase in plant capacities every year.

Geothermal energy is the energy obtained from the fluid, gas, and steam that have been stored in reservoirs by carrying the heat energy accumulated in the rocks in the depths of the earth or surfaced along the discontinuity zones. The increase in the use of geothermal energy and the increase in the capacity of the power plants has also revealed the problem of scaling. The main cause of deposition are the decrease in solubility of minerals by a decrease in pressure and temperature upon pumping the geothermal brine up to the ground. Calcium carbonate, calcium sulphate, metal silicates (Mg, Fe) are the most widely accepted types of scaling. In recent years, antimony and arsenic sulfide scaling have been encountered in volcanic and metamorphic regions. Between these two types of scaling, antimony sulfide is mostly seen in the heat-exchangers and preheaters where the temperature drops suddenly.

In this thesis, the antimony sulfide scaling formed in the geothermal power plant was synthesized in an autoclave reactor under specified conditions. Water-soluble polymers nominee for being antiscalants such as Poly (vinyl sulfonic acid), Poly (acrylamide-co-vinyl sulfonic acid), Poly (acrylamide-co-vinyl phosphonic acid), Alginic Acid, Natural antiscalants, Polyacrylic acid, and Polyvinyl alcohol were employed. The results suggest that polymers containing vinyl sulfonic acid and acrylamide likely shows remarkable progress in increasing the concentration of ions in decantate, particularly at low dosages. (≈ 5 ppm)

ÖZET

JEOTERMAL İKİLİ SİSTEMLERDE ANTİMON SÜLFÜR KABUKLAŞMASININ ENGELLENMESİ İÇİN YENİ BİR ANTİSKALANT GELİŞTİRİLMESİ

Fosil yakıtlı enerji kaynaklarının (doğal gaz, petrol ve kömür gibi) insan sağlığına ve doğaya verdiği zarardan dolayı son yıllarda yenilenebilir ve sürdürülebilir enerji kaynaklarına olan talebi artmaktadır. Jeolojik özellikleri nedeni ile Ülkemiz jeotermal enerji kaynakları bakımından zengin olduğundan her yıl santral kapasitelerinin de artışı söz konusudur.

Jeotermal enerji yerin derinliklerindeki kayalar içinde birikmiş olan ısı enerjisinin akışkanlarca taşınarak rezervuarlarda depolanmış veya süreksizlik zonları boyunca yüzeye çıkmış akışkan, gaz ve buhardan elde edilen enerjidir. . Jeotermal enerjinin kullanımının artması ve santral kapasitesindeki artış kabuklaşma problemini de ortaya çıkarmıştır. Kabuklaşmanın başlıca nedenleri yeraltında çözünen minerallerin akışkan yardımıyla yeryüzüne çıkarken basıncın, sıcaklığın ve pH' düşmesiyle çözünürlüklerinin azalmasıdır. Kalsiyum karbonat, kalsiyum sülfat, metal silikatlar (Mg,Fe) en yaygın olarak kabul edilen kabuklaşma türleridir. Son yıllarda volkanik ve metamorfik alanlarda antimon ve arsenik sülfür kabuklaşma türüne rastlanılmaktadır. Bu iki kabuklaşma türü arasında antimon sülfür genellikle ani sıcaklık düşüşlerinin gerçekleştiği ısı eşanjörü ve ön ısıtıcı da görülür.

Bu tezde, jeotermal santralde oluşan antimon sülfür kabuklaşması belirlenen koşullar otoklav reaktörde sentezlenmiştir. Poli (vinil sulfonik asit), Poli (akrilamid/vinil sulfonik asit), Poli (akrilamid/vinil fosfonik asit), Aljinik Asit, Doğal İnhibitör, Poliakrilik asit ve Polivinil alkol gibi su çözünür polimerler antiskalant olmak için aday olmuştur. Elde edilen veriler, vinil sulfonik asit ve akrilamid içeren polimerlerin özellikle düşük dozajlarda dekantanttaki iyon konsantrasyonunu arttırmada dikkate değer bir ilerleme göstermektedir.

Dedicated to my family...

TABLE OF CONTENTS

LIST OF FIGURES.....	ix
LIST OF TABLE.....	xii
LIST OF ABBREVIATIONS.....	xiii
CHAPTER 1. INTRODUCTION.....	1
1.1. Scaling Problem in Geothermal Binary Plants	1
1.2. Literature Review	2
1.2.1. Calcite (CaCO ₃), CaSO ₄ , and Ca ₃ (PO ₄) ₂ Scaling.....	2
1.2.2. Metal-Silicate Scaling.....	7
1.2.3. Antimony(III) – Sulfide Scaling.....	12
CHAPTER 2. EXPERIMENTAL	17
2.1. Reaction Mechanism	17
2.2. Materials and Methods	17
2.3. Characterizations of Artificial and Natural Deposits	18
2.4. Polymeric Antiscalants for Inhibitor Test	18
2.5. Characterization Tools.....	19
2.5.1. X-Ray Diffraction (XRD)	19
2.5.2. X-Ray Fluorescence (XRF).....	20
2.5.3. Fourier Transform Infrared Spectroscopy (FTIR).....	20
2.5.4. Inductively Coupled Plasma – Optical Emission Spectroscopy (ICP-OES).....	20
2.5.5. Scanning Electron Microscopy (SEM).....	20
CHAPTER 3. Results and Discussion.....	21
3.1. Structural, Morphological and Spectroscopic Analysis of Natural Deposit.....	21
3.1.1. XRD and XRF of Natural Deposits	21
3.1.2. SEM of Natural Deposits	22

3.1.3. FTIR Study.....	23
CHAPTER 4. SATURATION INDEX.....	25
4.1. Thermodynamic Aspect of Saturation Index.....	25
4.2. Saturation Index of Antimony Sulfide Scaling.....	26
CHAPTER 5. ARTIFICIAL DEPOSIT.....	28
5.1. Synthesis of Artificial Deposits.....	28
5.1.1. XRD of the Artificial Deposit.....	28
5.1.2. SEM of SbOCl Crsytals.....	29
5.1.3. Structural and Morphological Analysis of Artificial Stibnite Deposit.....	30
5.2. Screening Tests Using Polymeric Antiscalant.....	32
5.3. Structural and Morphological Analysis of Artificial Deposit After Addition of Various Polymeric Antiscalants.....	35
5.3.1. XRD Study.....	35
5.3.2. SEM Study.....	37
5.3.3. FTIR Study.....	38
CHAPTER 6. CONCLUSION.....	39
REFERENCES.....	40

LIST OF FIGURES

<u>Figure</u>	<u>Page</u>
Figure 1.1. Structures of being used chemicals and polymers as antiscalant (Source: Gill, 2008). ³	4
Figure 1.2. Synthesis scheme of (a) APEC and (b) AA/APEC antiscalants (Source: Fu et al. 2011). ¹³	5
Figure 1.3. Inhibition as a function of inhibitor dosage (Source: Fu et al. 2011). ¹³	6
Figure 1.4. Inhibition of calcium phosphate and calcium sulfate precipitation as a function of Ca ²⁺ ion concentration (a), PO ₄ ³⁻ or SO ₄ ²⁻ ion concentration (b), pH (c), and temperature (d) (Source: Fu et al. 2011). ¹³	7
Figure 1.5. Polycondensation mechanism of (a) amorphous silica and (b) metal silicates where M=Al, Fe (Source: Gallup, 2011). ¹⁵	7
Figure 1.6. Structures of silica dissolution chemical and polymeric additives (Source: Demadis et al. 2011). ⁶	9
Figure 1.7. Effect of chemical (PBTC and DETPA) dosages insoluble silica levels (Source: Demadis et al. 2011). ⁶	9
Figure 1.8. Changes after addition of different dosages of PBTC to Aerosil 200 and SSD silica (Source: Demadis et al. 2011). ⁶	10
Figure 1.9. Changes in silica soluble levels when PAMAM generations used (Source: Neofotistou and Demadis. 2004). ²⁰	10
Figure 1.10. Structures of (a) -NH ₂ terminated PAMAM, (b) Carboxymethyl inulin (CMI) (Source: Neofotistou and Demadis. 2004). ²⁰	11
Figure 1.11. The effects of different dosages of copolymer on the deposition (Source: Muller et al. 2015). ^{26, 27}	14
Figure 1.12. Sb recovery in different concentrations of NaOH at 295 K. (Source: SMINČÁKOVÁ and KOMOROVÁ. 2008). ²⁹	15

<u>Figure</u>	<u>Page</u>
Figure 1.13. The effect of different concentrations of mixed NaOH and Na ₂ S in Sb recovery, (1) 2wt.% NaOH, (2) 0.5wt.% Na ₂ S + 2wt.% NaOH, (3) 2wt.% Na ₂ S + 0.5wt.% NaOH and (4) 2wt.% Na ₂ S + 2wt.% NaOH (Source: SMINČÁKOVÁ and KOMOROVÁ. 2008). ²⁹	16
Figure 2.1. Experimental set-up for Stibnite synthesis	18
Figure 2.2. Chemical structures of polymeric antiscalants.....	19
Figure 3.1. XRD results of low pressure (LP) and high pressure (HP) area samples....	21
Figure 3.2. SEM images of deposits obtained from High and Low-Pressure areas (×25k).....	22
Figure 3.3. FTIR spectrum of HP, LP, and Natural inhibitor	23
Figure 4.1. Stibnite solubility diagram at different H ₂ S concentrations	27
Figure 5.1. XRD patterns show from bottom to top 500ppm, 1000ppm, 5000ppm, and 10g/L reactions at 80°C.....	28
Figure 5.2. SEM images of the synthesized precipitates (a) 500 ppm ×10k. (b) 1000 ppm ×10k. (c) 5000 ppm ×10k. And (d) 10 g/L ×25k. at 80°C, 2h using reflux system.	29
Figure 5.3. X-Ray Diffractogram of the precipitates prepared at various reaction times.....	30
Figure 5.4. Photographs show that the color-changing a) 12h at 137°C (3 bar) black-greyish stibnite crystals, b) 2h at 137°C (3 bar) antimony trioxide reddish-brown particles.	31
Figure 5.5. SEM images of 2h (Sb ₂ O ₃), 4h, 8h, 12h, 16h stibnite crystals (×25k).....	31
Figure 5.6. ICP-OES results show the change in [Sb ³⁺], [Na ⁺], and [S ²⁻] concentrations in the presence of 25, 50, and 100 ppm dosage of antiscalants and the control sample refers to blank solution.	33
Figure 5.7. X-ray Diffractogram of inhibited powder in the presence of 100 ppm dosage of PAM-co-VSA, PVSA, and Polyacrylic Acid	35

LIST OF TABLES

<u>Table</u>	<u>Page</u>
Table 3.1. XRF results of high and low-pressure area samples.....	22
Table 3.2. EDX results of the sample which were taken from a high and low-pressure area	23
Table 3.3. Represents IR transmission bands in natural inhibitor, HP, and LP samples.....	23
Table 5.1. Represents the percent inhibition efficiencies of [Sb ³⁺] concentration in the presence of 5, 25, 50 and 100 ppm inhibitor dosage.....	35

LIST OF ABBREVIATIONS

XRD	X-Ray Diffraction
SEM	Scanning Electron Microscopy
ICP-OES	Inductively Coupled Plasma Optical Emission Spectroscopy
XRF	X-Ray Fluorescence
FTIR	Fourier Transform Infrared Spectroscopy
HP	High Pressure
LP	Low Pressure
EDX	Energy-Dispersive X-Ray Spectroscopy

CHAPTER 1

INTRODUCTION

1.1. Scaling Problem in Geothermal Binary Plants

Geothermal energy is a renewable, clean, inexpensive, and environmentally friendly energy source. It is localized to some regions of the world. Turkey is one of the important regions that have high geothermal activity. However, serious scaling problems are encountered when geothermal brine is brought to atmospheric conditions. Various types of scaling are observed in geothermal plants depending on the geological features of the region of interest, such as calcite, calcium sulfate, calcium fluoride, magnesium fluoride, magnesium silicate, opaline silica, iron-magnesium-silicates, and metal-sulfides.¹ Among them, calcite, calcium sulfate, magnesium silicate, and metal-sulfides are the most commonly observed deposit chemistries. The occurrence of scaling depends on various parameters such as pH of brine, temperature change, pressure, degree of supersaturation, and the composition of the brine. The formation of incrustation of carbonates like CaCO_3 , MgCO_3 , BaCO_3 , and SrCO_3 depends on changing the brine pressure and pH. Decreasing the pressure results in CO_2 release and pH increasing. Since CO_2 has an acidic nature, the disappearance of CO_2 yields increased pH. Thus, calcite solubility decreases with increasing the temperature and decreasing the pressure.^{2, 3} Changes in the same parameters, such as carbonates, also cause the sulfate precipitation. If two different waters chemically interact with each other, sulfate scaling begins. When a watery system consists of Ba^{2+} , Ca^{2+} , Sr^{2+} mixed with sulfate-rich water, BaSO_4 , SrSO_4 , and CaSO_4 are likely to precipitate.⁴

Considering the metal-silicate deposition, the location of scale can be seen in both production and injection wells. The decrease in the temperature and pressure results in a serious scaling problem. Scaling can be observed in heat-exchangers, pipes, and separator vessels, and it causes significant fouling of the system. When the system

begins fouling, the energy production decreases.⁵ Thus, dissolution of silicate was tested in the presence of various polymeric antiscalants and HF for energy increasing.⁶⁻⁸

Metal-sulfide scaling has been seen in both low and high enthalpy fluids. The scale not only consists of the huge amount of dissolved Fe^{2+} but also includes Pb^{2+} , Zn^{2+} , Au^+ , and Ag^+ .⁹ However, over the past ten years, a new metal-sulfide scaling was encountered called antimony trisulfide, stibnite. It is a black-grayish deposit and is seen in preheaters where the temperature drops suddenly from high to low.¹⁰

Carbonates, sulfates, metal-silicates, and metal-sulfides are well-known geothermal deposits, and their formation is minimized by polymeric antiscalant trials or commercial products. Stibnite scaling is also solved with commercial products, but to the best of our knowledge no specific effective antiscalant chemistry is suggested in the literature according to the best of our knowledge.

In this thesis, antimony sulfide (stibnite) crystals were synthesized by using autoclave, which reaches high temperatures and pressures as in the field of the geothermal power plant. After the scale was synthesized artificially in the lab, starting from SbCl_3 and Na_2S , various types of water-soluble polymers were tested. Success criteria were the decreasing amount of deposit and increasing the concentration of the ions in the decantate, which is the leftover solution after the precipitation of the sulfur-rich deposit. The polymers used for testing in this work had a functional group, for instance, acrylamide and sulfonic acid.

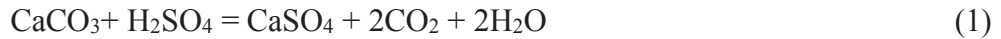
1.2. Literature Review

In this section, the related papers about various types of scaling problems and their mitigation studies will be presented.

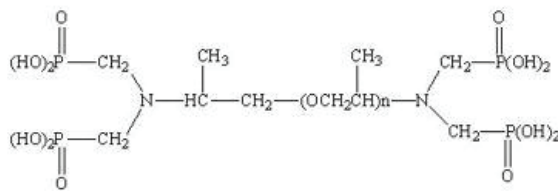
1.2.1. Calcite (CaCO_3), CaSO_4 , and $\text{Ca}_3(\text{PO}_4)_2$ Scaling

Calcite scaling became a severe problem in the past. It has generally been observed in geothermal systems in the form of CaCO_3 , CaSO_4 , and $\text{Ca}_3(\text{PO}_4)_2$.^{2, 11} The most common deposit was CaCO_3 , particularly calcite. When CO_2 releases during brine flashes, pressure drops, and this causes an increase in pH and temperature. Changes in parameters cause the ideal media for calcium carbonate precipitation.³

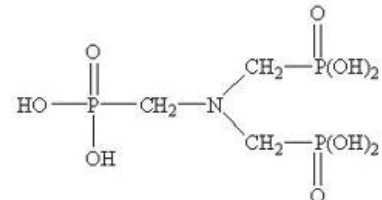
To prevent calcite scaling, the first thing is to control pH. The addition of sulfuric acid, which is cost-efficient, inhibits the calcium carbonate scaling. It decreases the alkalinity (media become slightly acidic), and this time, calcium sulfate precipitation, which is more soluble than calcium carbonate, has occurred. However, sulfuric acid should be added in a controlled process because excess SO_4^{2-} causes a corrosive effect.^{3, 11} The reaction between H_2SO_4 and CaCO_3 is shown below.



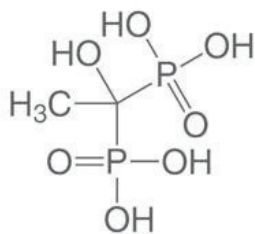
Another and most useful technique for preventing calcite scaling is to use polymeric antiscalants. The effect of antiscalant on calcium carbonate was investigated. In the first part, polyacrylamide (PAA) and polyamino polyether methylene phosphonate (PAPEMP) were used for the inhibition test. Various concentrations (0.5, 1, 1.5, 2, 3 ppm) of the antiscalant were added to the system. The results show that the addition of 2.5 ppm PAPEMP gave the highest inhibition efficiency at 95%, and when 3 ppm PAA was added, the inhibition efficiency became 85%. Even sulfuric acid also yielded promising results for inhibition, given that damage to the surface of pipes was high. Thus, it has not preferred to use as an inhibition product.^{3, 11, 12}



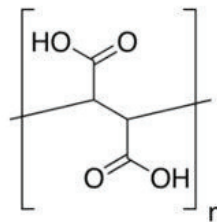
Polyamino polyether methylenephosphonic acid
(PAPEMP)



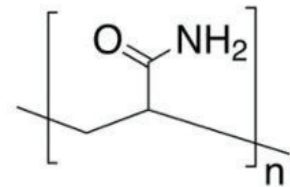
Amino tri(methylene phosphonic acid)
(AMP)



1-Hydroxyethylidene 1-1 diphosphonic acid
(HEDP)



Polymaleic acid (PMA)



Polyacrylamide (PAA)

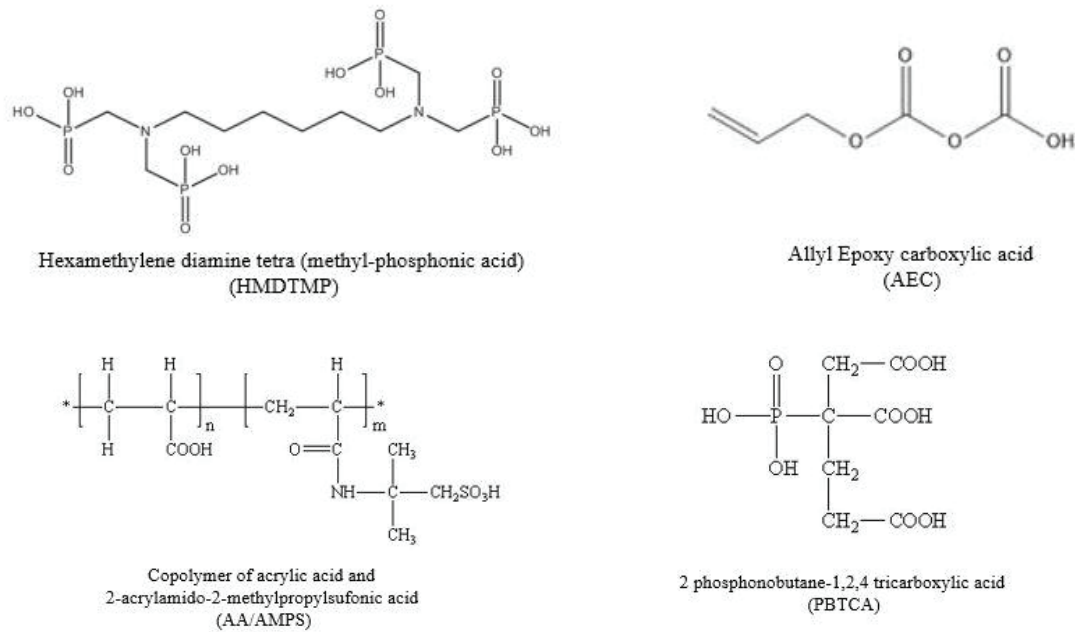


Figure 1.1. Structures of being used chemicals and polymers as antiscalant (Source: Gill, 2008).³

The antiscaling effect of PAPEMP suggests positive results. This time, in addition to PAPEMP, six more polymers were tested for the mitigation process. A 25 ppm dosage of AMP, HMDTMP, PBTCa, PAPEMP, PMA, AEC, and a 23.4 ppm dosage of HEDP-AMP-AA/AMPS copolymer was used at pH 9.0 and temperature 55°C. Inhibition efficiency values were calculated at 41, 55, 57, 100, 56, 62 and 60% respectively. From those, PAPEMP gave the highest efficiency. Also, the second trial was tested for both calcium carbonate and calcium sulfate scaling at pH 7.5, 250°C, and SO₄ concentration was 1500 ppm. PAA, PMA, and PAPEMP-AA/AMPS were used in different dosages at 5 and 10 ppm and inhibition tested in different calcium concentrations. Antiscaling efficiency was calculated, and PAPEMP-AA/AMPS gave the highest inhibition efficiency at 50, 100, and 500 ppm calcium levels at 100%, and at the 1000 ppm calcium level, 5 and 10 ppm dosages inhibited 72 and 89%, respectively. Thus, in different concentrations, the effect of mixed polymers was better for inhibition chemistry of CaCO₃ and CaSO₄ precipitation.³

Moreover, increasing the effectiveness of polymeric antiscalants depends on chain length. The shorter the chain length, the better the effectiveness of the polymer. Also, the use of low molecular weight (<50,000) polyacrylates and organophosphorus compounds is better for the inhibition process. The inhibition process, which is between polymeric antiscalant and deposits, was explained. Antiscalants block the crystal from

the growing site, and dissolution begins. This may be because the electrostatic force of ionic charges in the polymer interacts with the scale. Since this process is adsorption, it is reproducible about 10 times.¹¹

Except for PAPEMP, a different polymer called AA (acrylic acid)/APEC (allylpolyethoxy carboxylate) was synthesized in Fig 1.2. In this study, PAPEMP and AA/APES (allylpolyethoxy sulfate) were used as reference antiscalant inhibitors. For calcium phosphate inhibition in Fig. 1.3. pH and temperature were adjusted 9.0 and 80°C for 10 h. The dosage of 2 and 6 ppm AA/APEC was used, and the inhibition efficiency was changed from 29.56 to 99.59, respectively. Comparing AA/APEC and AA/APES, from both polymers, the addition of 8 ppm dosage showed the different inhibition efficiency as 99.89 and 80.13%. When 8 ppm PAPEMP was used, the inhibition decreased to 29.89%. However, increasing the addition of PAPEMP concentration about 25 ppm increases the calcium phosphate inhibition to 92%, but using high concentrations is not economical.

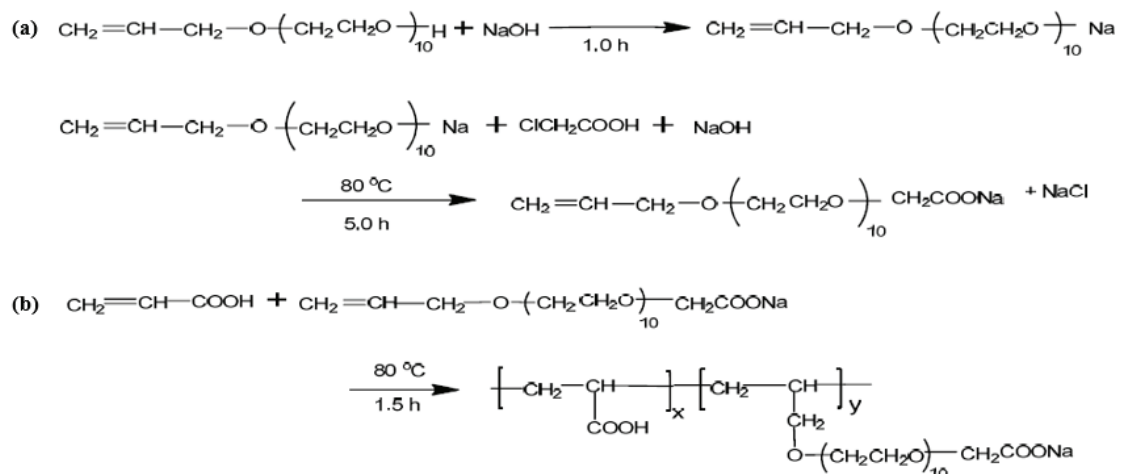


Figure 1.2. Synthesis scheme of (a) APEC and (b) AA/APEC antiscalants (Source: Fu et al. 2011).¹³

To see the effect of these three inhibitors on calcium sulfate, pH and temperature were adjusted 7.0 and 80°C for 12 h. When these three polymers were compared at threshold dosages, AA/APEC showed a better result than PAPEMP at 81 and 91%, respectively. On the other hand, AA/APES gave the lowest inhibition efficiency result at the same threshold dosage shown in Fig. 1.3.

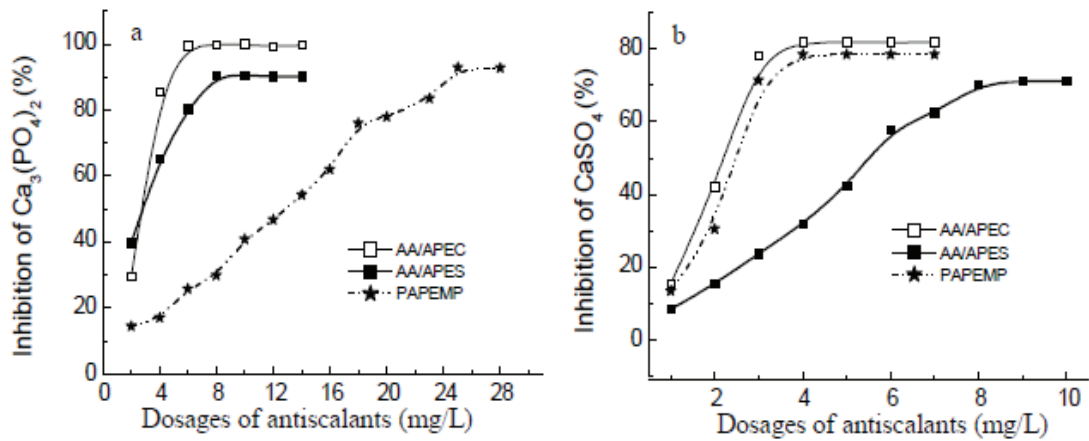
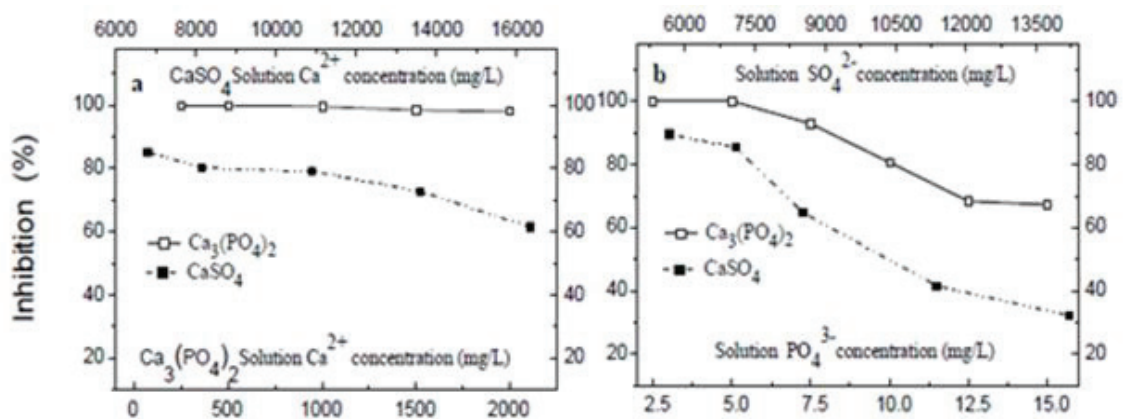


Figure 1.3. Inhibition as a function of inhibitor dosage (Source: Fu et al. 2011).¹³

Various parameters were used to determine whether AA/APEC is effective against $\text{Ca}_3(\text{PO}_4)_2$ and CaSO_4 inhibition in different conditions. The increase in Ca^{2+} , PO_4^{3-} , and SO_4^{2-} concentration levels, temperature, and pH were examined in Fig. 1.4.

Figure 1.4(a) shows in the presence of AA/APEC, and as the calcium concentration in $\text{Ca}_3(\text{PO}_4)_2$ and CaSO_4 increase, calcium sulfate inhibition decreases while calcium phosphate inhibition remains unchanged. Figure 1.4(b) demonstrated that when SO_4^{2-} and PO_4^{3-} ion concentration increases, the inhibition efficiency of AA/APEC decreased. Figures 1.4(c) and 1.4(d) reveal how AA/APEC acts in pH and temperature change. From the 3-11 pH values, $\text{Ca}_3(\text{PO}_4)_2$ shows a better inhibition reaction, whereas CaSO_4 showed better between 5-11. The increase in the temperature also showed better inhibition efficiency for calcium phosphate. From those results, AA/APEC has a good inhibition reaction against both CaSO_4 and $\text{Ca}_3(\text{PO}_4)_2$ scaling.¹³



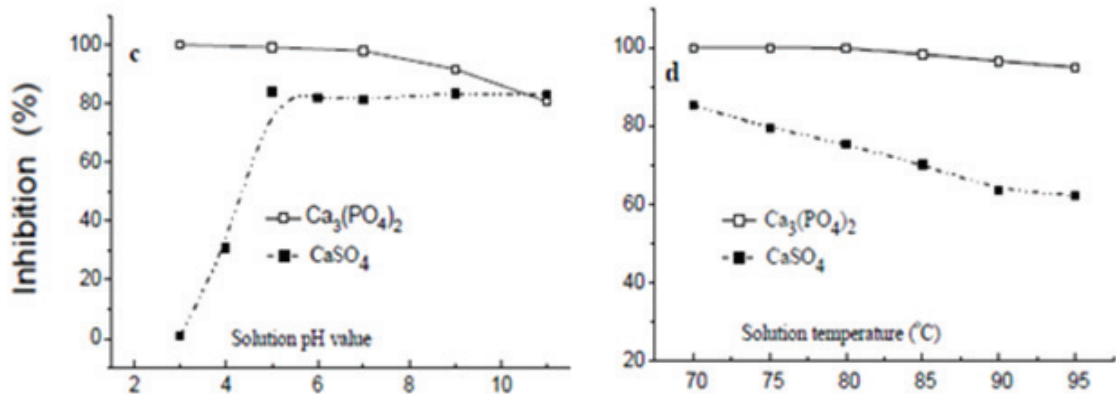


Figure 1.4. Inhibition of calcium phosphate and calcium sulfate precipitation as a function of Ca²⁺ ion concentration (a), PO₄³⁻ or SO₄²⁻ ion concentration (b), pH (c), and temperature (d) (Source: Fu et al. 2011).¹³

1.2.2. Metal-Silicate Scaling

Metal-silicate deposition is observed in pipelines, heat-exchangers, and separators, and it became a significant problem for geothermal plants.^{14, 15} The most common metal-silicate compounds consist of Al (aluminum), Mg (magnesium), and Fe (iron) in geothermal water. Iron and magnesium silicate show poor solubility in low temperatures, whereas aluminum-silicate deposition occurs at high temperatures.^{16, 17} The reason is that, during the production, when brine flashes, temperature and pressure drop; dissolved CO₂ is released from the system, and pH increases. Thus, situation prepares a convenient media for metal-silicate deposition.^{5, 12}

Silica presents a different form in nature, such as quartz, tridymite, cristobalite, opal A (amorphous silica).^{14, 18} Quartz is the most common form in nature. Although quartz and other crystalline silica's have a slow deposition rate, amorphous silica precipitates fast by polycondensation.^{5, 15, 16}

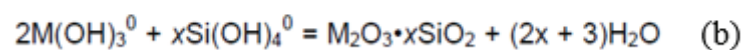
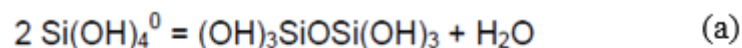
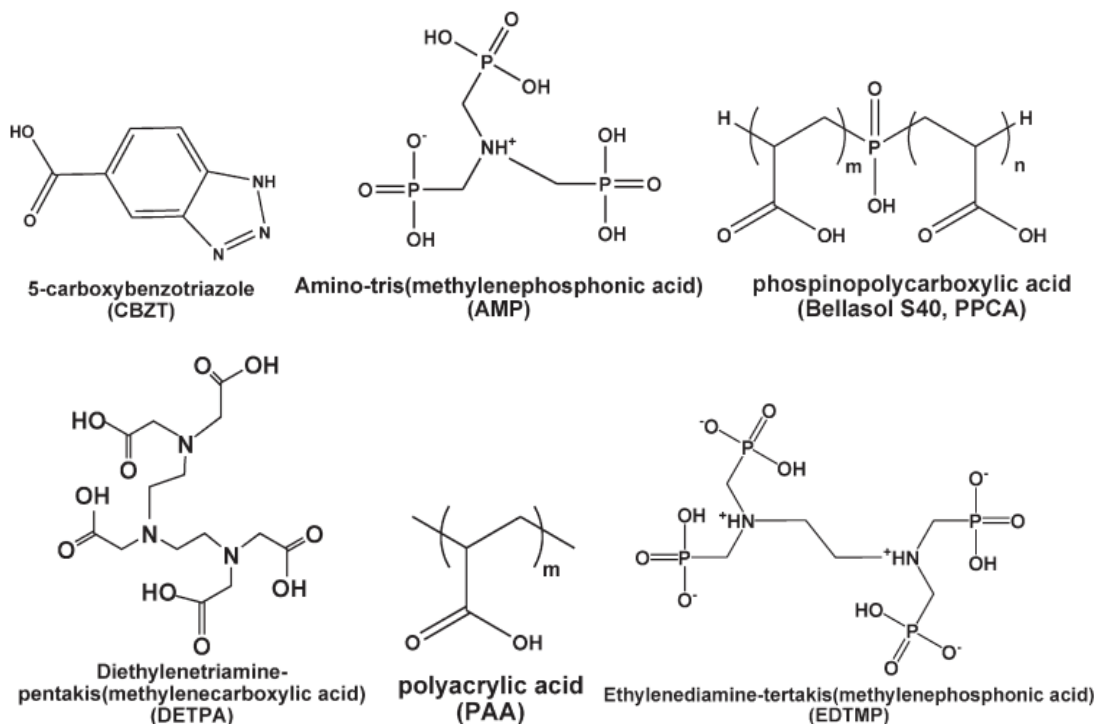


Figure 1.5. Polycondensation mechanism of (a) amorphous silica and (b) metal silicates where M=Al, Fe (Source: Gallup, 2011).¹⁵

Moreover, magnesium-silicate scaling also occurs in the binary systems. Just like pure silica, the magnesium-silicate system is also pH-dependent. Under pH 7, there is no deposition reaction occurs between silica and Mg^{2+} ions because silica appears as a non-ionic form at lower pH levels. At higher pH between 8.5 to 10, silicic acid $[Si(OH)_4]$ loses a proton, and it turns to silicate form $[Si(OH)_3O^-]$. After deprotonation, silicate shows more reactivity against Mg^{2+} ions because of electrostatic forces, so precipitation occurs quickly.^{16, 17}

For inhibition of metal-silicates, some solutions were found in the literature. HF is well known as a strong acid, and it is very effective against silicate dissolution. It breaks the Si-O bond easily, but its' corrosive effect is high on the metal surface.^{1, 8, 19} In Turkey, the Tuzla Geothermal Field (TGP), which is known for its high salinity, faces a metal-silicate problem. The plant temperature is $173^{\circ}C$, and because of the deposit, there is a blockage seen from pipelines. This blockage causes heat loss, and economic loss increases. Mechanical cleaning was tried, but it was still not a logical method for the cleaning process. However, the problem was solved by a using weak organic acid called formic acid. It is environmentally friendly, and it does not cause corrosion when it is added in a controlled way.^{1, 17}



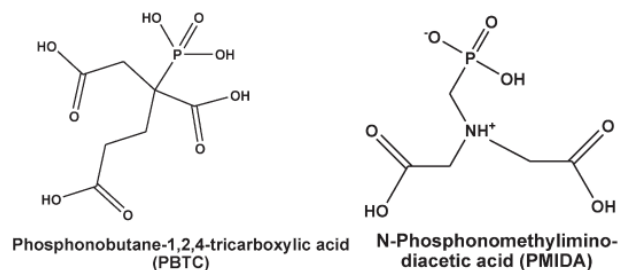


Figure 1.6. Structures of silica dissolution chemical and polymeric additives (Source: Demadis et al. 2011).⁶

Figure 1.6 shows the effect of chemical additives on artificial colloidal silica deposits called Aerosil 200 and synthetic silicon dioxide at pH 10. At first, the inhibition efficiency of these chemical inhibitors was tested with different dosages of 2500, 5000, 7500, and 10000 ppm on Aerosil 200, and these tests were carried on for 24, 48, 72h, respectively. The results show that AMP, PMIDA, and PAA are not effective against the dissolution of silica. Using PAA shows that the soluble silica level is worse than the control sample. After 72h, the addition of higher than 5000 ppm of PPCA reaches about 250 ppm silica dissolution. Using 10 000 ppm dosage of Genesol 40 gave the best result after 72h, approximately 290 ppm silica dissolution. When comparing EDTMP and CBZT, both are effective when used at low dosages (2500 ppm), but CBZT is not as good as EDTMP. The soluble silica levels increased 300 ppm and 240 ppm, respectively. The 5000 ppm dosage of sodium metaborate shows good solubility on silicic acid about 250 ppm, but increasing the dosage cannot increase the solubility performance. The last and the most effective antiscalant, PBTC and DETPA, was investigated on the dissolution of silica. Both demonstrate an excellent result at 7500 ppm dosages, as shown in Fig. 1.7.

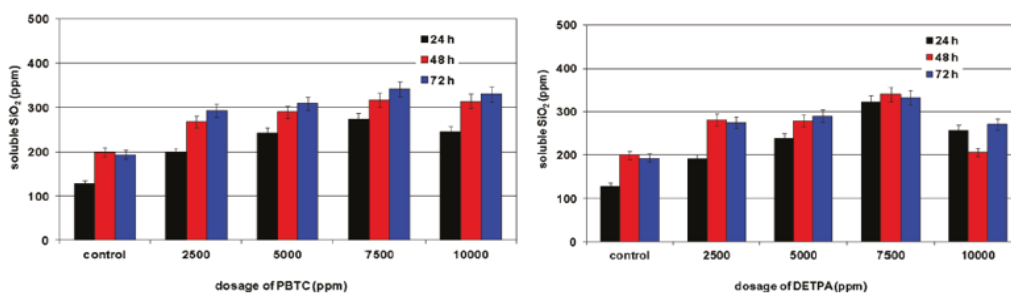


Figure 1.7. Effect of chemical (PBTC and DETPA) dosages insoluble silica levels (Source: Demadis et al. 2011).⁶

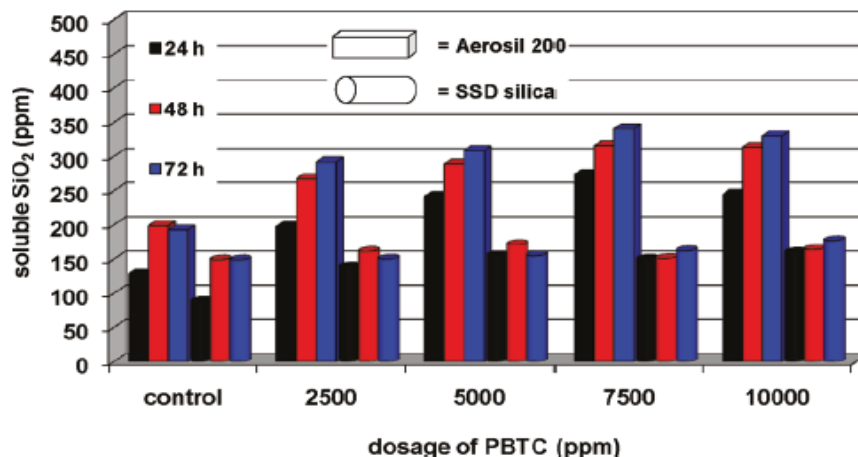


Figure 1.8. Changes after addition of different dosages of PBTC to Aerosil 200 and SSD silica (Source: Demadis et al. 2011).⁶

Since PBTC has a good dissolution agent and increases the Aerosil 200 solubility in low dosages better than DETPA, its' solubility in the synthetic sample was also compared in Fig. 1.8. Under the same conditions, after 24 h, Aerosil 200 silica solubility became 130 ppm, whereas it was 90 ppm in SSD. At high dosages (7500 ppm), SSD solubility was 180 ppm, and Aerosil was 330 ppm after 72 h. This is because the SSD particles are much denser than Aerosil 200 silica, and the effectiveness of particle covering is easy in Aerosil 200. The results showed that only the COOH or PO₃H₂ groups do not have a severe dissolution efficiency. However, if both functional groups are in the same molecule, the dissolution efficiency increases both low and high dosages.⁶

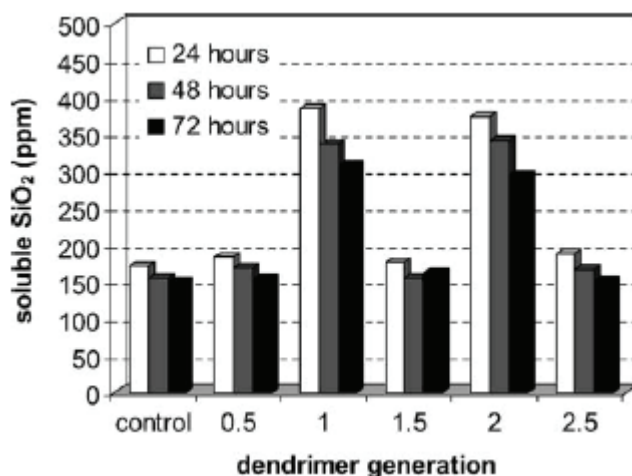


Figure 1.9. Changes in silica soluble levels when PAMAM generations used (Source: Neofotistou and Demadis. 2004).²⁰

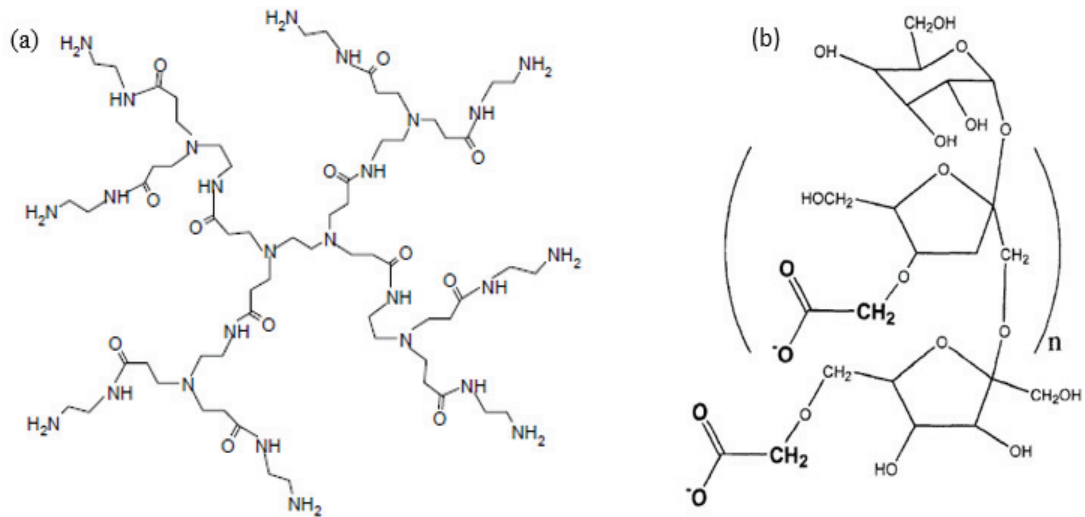


Figure 1.10. Structures of (a) -NH₂ terminated PAMAM, (b) Carboxymethyl inulin (CMI) (Source: Neofotistou and Demadis. 2004).²⁰

PAMAM dendrimers (-COOH and -NH₂ termini) were tested for silicate inhibition. Generation 1 and 2 PAMAM is NH₂ terminated, and 0.5, 1.5, 2.5 is -COOH terminated structures. The solution pH is adjusted to 7. Fig. 1.9. shows the soluble silica levels in the presence of 40 ppm dosage of PAMAM generations after 24, 48, and 72 h.

After 24 h, PAMAM-1 and PAMAM-2 show higher soluble silica performance of 384 and 374 ppm, respectively. At 48 and 72 h., the loss of inhibitor performance was noticed. Comparison with NH₂ and -COOH terminated PAMAM, -COOH one caused only a small amount of silica inhibition. Due to the charge repulsion between COO⁻ and silicate (anionic silica), -COOH terminated PAMAM is ineffective against the dissolution of silica. However, in NH₂-terminated PAMAMs, protonated NH₃⁺ groups attack the silicate ions and stop the particle growth very effectively.^{20, 21}

Moreover, PAMAM-1 increases the soluble silica level better than PAMAM-2. However, when the PAMAM generations react with SiO₂, PAMAM-SiO₂ deposition forms, and flocculation occurs. Thus, CMI, which is known as anionic polyelectrolyte (-COO⁻), was used for neutralizing -NH₃⁺ groups on dendrimers. The reason for this is to protect dendrimers from being associated with colloidal silica matrix. Also, the results showed that the addition of excess dosage of CMI (above 40 ppm) decreases the inhibition activity.²⁰

1.2.3. Antimony(III) – Sulfide Scaling

Antimony forms as an oxidation state of +3 and +5 in nature. In geothermal binary systems, oxidation state of Sb^{3+} is commonly seen. In heat-exchangers, where the temperature drops from high to low, the black-greyish (crystalline) precipitate forms. The stibnite scale is also pH-dependent, and at lower pH, precipitation occurs fast. It is insoluble in water ($K_{sp}: 1.6 \times 10^{-91}$), and scale obstructs the heat-exchangers, which causes great production loss.²²⁻²⁵ The dissolution of stibnite in water was written as below;



In this reaction, antimony hydroxide acts as an acid, and it's called antimonous acid. The dissociation reaction of antimonous acid explained below;



Also, the dissociation of antimonous acid in water is written as;



Also, at 25°C, the pH of this reaction is 12, and the concentration of both H_3SbO_3 and H_4SbO_4^- are nearly equal concentrations. An increase in pH triggers the more antimonous acid to transform anion form. The more anion form occurs, the more solubility in water increases. Stibnite dissolves in solutions where the H_2S concentration is high. The resulting product is $\text{H}_2\text{Sb}_2\text{S}_4$, which is known as thioantimonite, and it dissociates easily in an alkaline solution.²³



Furthermore, the deposition occurs when the pH becomes slightly basic. When the pH is 8 and the temperature is $<100^{\circ}\text{C}$, stibnite can readily precipitate. Although the total concentration of antimony is lower than 1-2 ppm in brine, it precipitates very quickly in heat-exchangers. For dissolution of stibnite, HCl or other strong acids was used, and the reaction between acid and stibnite produced H_2S gas, which is toxic for human health.²⁴

In the winter of 2014, the system in Germencik (Western Turkey), shut down due to loss of energy production, and heat-exchangers were opened. A black-greyish precipitate (1-4 mm) was seen, and the thickness of scale was smaller in preheaters than in vaporizers (4-5 mm), but it is much harder and denser. It was observed that the color of the precipitate was changed towards the preheaters from purplish to reddish-orange. The deposit was analyzed, and it was found to be black-crystalline and red-amorphous stibnite. Even with its color changes in preheaters, it was still antimony sulfide scale.^{10,}
²⁵ For mitigation of antimony, some solutions are suggested. For example, avoiding low temperatures would be the one solution, but it causes loss of production. Normally, the reason for the low pH is the dissolved gas (CO_2) in brine. Thus, if this gas is purged, the scale problem could be solved. Considering the mechanical and chemical removal of deposits, both are time-consuming and cause loss of production. Moreover, caustic washing is very effective, but it is not economically friendly. Also, polymeric antiscalants were tested for the inhibition process. Three different polymers were used, and their inhibition and dispersion effects were compared. Five ppm of GEO 903 (homopolymer), ScaleGuard 60123 (copolymer), and 10 ppm of 5200M (mix of phosphonate and a copolymer) were used for stibnite inhibition, and the efficiencies are 83, 90, and 56%, respectively. Commonly, 5200M is known as a standard calcite inhibitor, and it was not effective against stibnite inhibition. Antimony particles smaller than 0.2 microns were considered as soluble antimony. Thus, low molecular weight polymers ($<20,000$) with high anionic charge density are very effective in making particle size smaller. Therefore, they were better than phosphonates. Moreover, the same dosage of inhibitors was used for understanding the dispersion effect. The result showed that the dispersion efficiencies were calculated at 93, 95, and 60%, respectively. Considering both, performance copolymer ScaleGuard 60123 was better for stibnite inhibition.^{23, 24}

$$\% \text{ Dispersion} = (\text{T}_f \text{ Blank} - \text{T}_f \text{ Sample}) / (\text{T}_f \text{ Blank} - \text{T}_i \text{ Blank}) \times 100 \quad (8)$$

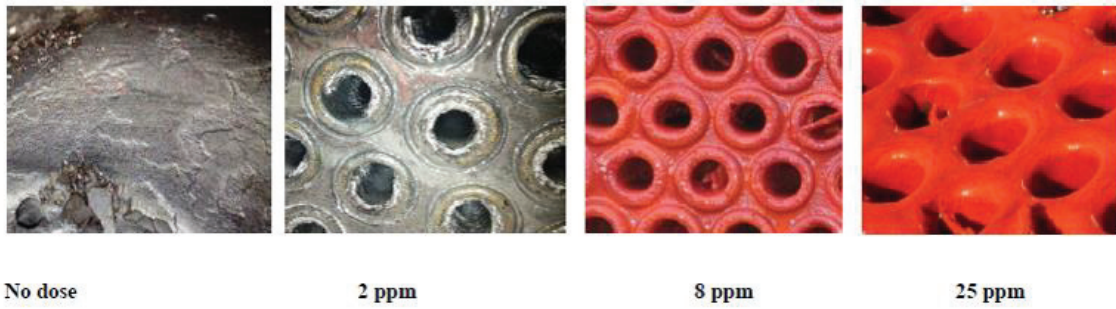


Figure 1.11. The effects of different dosages of copolymer on the deposition (Source: Muller et al. 2015).^{26,27}

A copolymer was tested for the inhibition process in the geothermal field. Different dosages of the copolymer (2, 8, and 25 ppm) were tested to see how it affects the deposition represented in Figure 1.11. Without any dosage, it was seen as crystalline stibnite. After a dosage of 2 ppm of copolymer, it became softer and easy to remove from the system. The addition of high dosages changes the color from dark-grey to crimson-red (colloidal), and it looks more gelatinous. However, using high dosages of copolymer caused a decrease in pressure and heat-exchangers. It was clear that even using the low dosages gave better performance according to high dosages. In stibnite inhibition, considering the chemistry of copolymer, polycarboxylates and specific M_w of carboxylic acids are better for the removal of antimony from its crystalline structure. The chelating effect depends on brine pH, and at high pH, deprotonation of acidic groups resulted in high anionic charged groups, which keeps antimony particles smaller.^{26,27}

Dissolution of stibnite in alkaline solutions was also tested. At first, acids such as the mixture of hydrochloric-tartaric acid, nitric-tartaric acids, and concentrated sulfuric acid were used. However, alkaline sulfide compounds are well-known leaching agents as dissolution of antimony. The following equations show the reaction of stibnite in alkaline sulfide solutions.²⁸⁻³¹



So, the duty of NaOH is to prevent the hydrolysis of Na_2S . The process is shown in steps 9 and 10.



The total reaction of step 9 and 10 is given below;



Moreover, reaction 12, 13, and 14 demonstrates stibnite dissolution in aqueous NaOH solution



These reactions (8, 12, 13, and 14) in the dissolution of stibnite in alkaline solutions result in the different kinds of water-soluble antimony compounds such as antimonites, thioantimonites, and oxothioantimonites. The natural stibnite deposit was used for the dissolution process. For each trial, a 0.4 g sample was used. The reaction was maintained in 200 ml of glass reactor, and the temperature was controlled at 298, 323, and 348 K, respectively. Different concentrations of NaOH and mixed NaOH-Na₂S solution were tested for Sb recovery, shown in Figures 1.12 and 1.13.

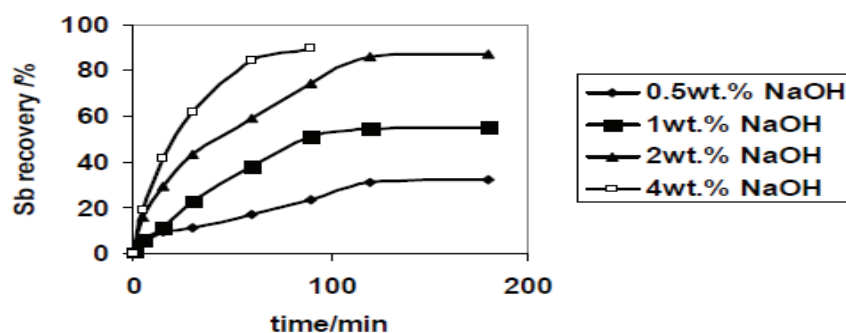


Figure 1.12. Sb recovery in different concentrations of NaOH at 295 K. (Source: SMINČÁKOVÁ and KOMOROVÁ. 2008).²⁹

Results showed that until 90 min., the highest Sb recovery is 4% wt. NaOH. After 90 min., the recovery stops, and antimony did not dissolve more in the solution. At long periods, increasing the concentration increases the percent Sb recovery (addition of 2% wt. NaOH causes 74.2 % Sb recovery)

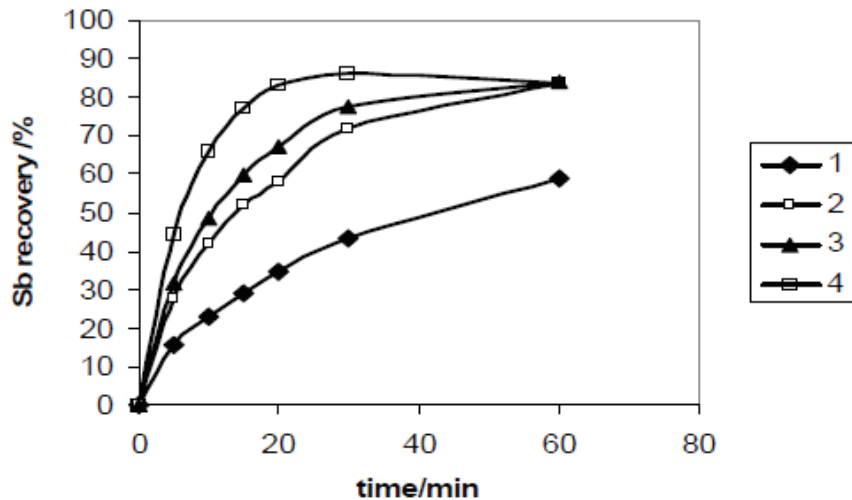


Figure 1.13. The effect of different concentrations of mixed NaOH and Na₂S in Sb recovery, (1) 2% wt. NaOH, (2) 0.5% wt. Na₂S + 2% wt. NaOH, (3) 2% wt. Na₂S + 0.5% wt. NaOH and (4) 2% wt. Na₂S + 2%wt. NaOH (Source: SMINČÁKOVÁ and KOMOROVÁ. 2008).²⁹

Considering the mixed solutions, 2% wt. Na₂S + 2% wt. NaOH gave the highest Sb recovery (86%) until 30 min. However, after 30 min., the leaching period did not give a better result. Compared with 2% wt. Na₂S + 0.5% wt. NaOH and 2% wt. NaOH + 0.5% wt. Na₂S, the initial Sb recovery is higher in a mixed solution of (3), but at 60 min, the Sb recoveries were the same at 84%. Thus, in both results, the long periods did not show good Sb recoveries.

CHAPTER 2

EXPERIMENTAL

2.1. Reaction

In this reaction antimony trichloride and sodium sulfide trihydrate are the reactants. The resultant product assumed to be antimony trisulfide.



2.2. Materials and Methods

To synthesize artificial stibnite deposits, an autoclave (Buchiglasuster, Switzerland) was used. This autoclave consists of three important parts: the circulator, the main part, and the monitor. The circulator is used for silicon oil to increase the temperature up to 200°C. The main part of the autoclave is where the reaction starts, and the monitor shows the pH, temperature, and RPM values. A total of a 1000 ppm reaction was prepared³¹. 103 mg SbCl₃ (Sigma Aldrich ACS reagent, >99.0%) and 97 mg of Na₂S·3H₂O were dissolved into 130 ml and 70 ml of ultrapure water (18.2 MΩ·cm⁻¹ at 25 °C). After both were stirred for one hour in different beakers, they were added to the autoclave (Fig. 3.1), and the reaction started. The reaction continued at 137.5°C (3 bar) for about 12h. After 12h, the black-crystalline product was obtained in an ice bath. After cooling, it was centrifuged for 15 min. at 6000 RPM. After the centrifuge finished, the decantate and solid product were removed from each other. The solid product was put into a vacuum oven at 60°C for approximately 12h for x-ray diffraction (XRD) analysis. The decantate was acidified with 2% HNO₃ for ICP-OES analysis.

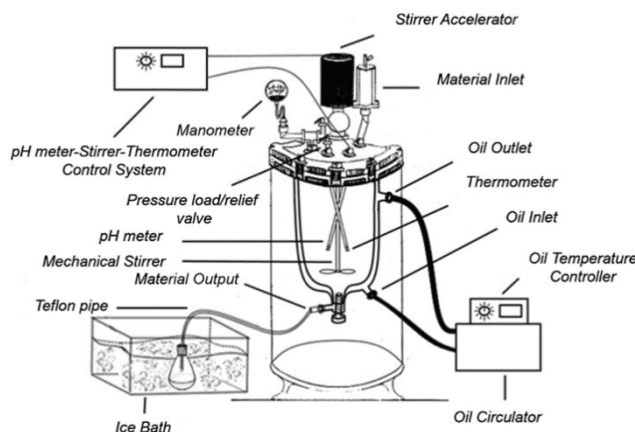


Figure 2.1. Experimental set-up for Stibnite synthesis

2.3. Characterizations of Artificial and Natural Deposits

Both natural and artificial deposits were powdered in a ceramic container for characterization with x-ray fluorescence (XRF), Fourier transform infrared (FTIR), x-ray diffraction (XRD), and scanning electron microscopy (SEM). XRF(Spectro iQ II, Kleve, Germany) shows us the % elemental composition in the deposits. With SEM (FEI Quanta 250 FEG, Oregon, USA), the crystallographic morphology can be analyzed. Fourier transform infrared spectroscopy (Perkin Elmer) is a method that obtains an absorption or emission of a solid, liquid, or gas matters. X-ray Diffraction(XRD; PhilipsX'Pert Pro, Eindhoven, The Netherlands) helps find the crystal structure of a deposit.

2.4. Polymeric Antiscalants for Inhibitor Test

Antiscalants are commercial products used to disrupt the crystal structure of stibnite. For the testing, artificial brine was prepared.³² An amount of 107 mg SbCl_3 and 93 mg $\text{Na}_2\text{S} \cdot 3\text{H}_2\text{O}$ are both dissolved differently in 130 ml and 60 ml of deionized water. The remaining 10 ml was prepared to dissolve the inhibitor. For each inhibitor, three trials were made at 25 ppm, 50 ppm, and 100 ppm. First, SbCl_3 and $\text{Na}_2\text{S} \cdot 3\text{H}_2\text{O}$ were added to the autoclave. After that, polymeric antiscalant was added to the system. The reaction continued for 12 h. at 137.5°C (3 bar). When the reaction ended, the sample was taken to the ice bath for a cooling process of about 30 min. After cooling, it

was centrifuged for 15 min at 6000 RPM. Later, solid and decantate were separated from each other. The solid sample was put into the vacuum oven at 60°C for 12h., and the decantate was acidified with 2% (v/v) HNO₃ for ICP-OES analysis. According to reference, ICP-OES results and initial and final mass of the solid deposit were compared. Solid was analyzed with FTIR and XRD. The FTIR spectrum hints about whether the solid includes a polymeric inhibitor or not. If the mass is increased, we can understand that the solid includes a polymer. The XRD pattern also demonstrates how its crystallographic structure changes after the addition of polymeric antiscalants.

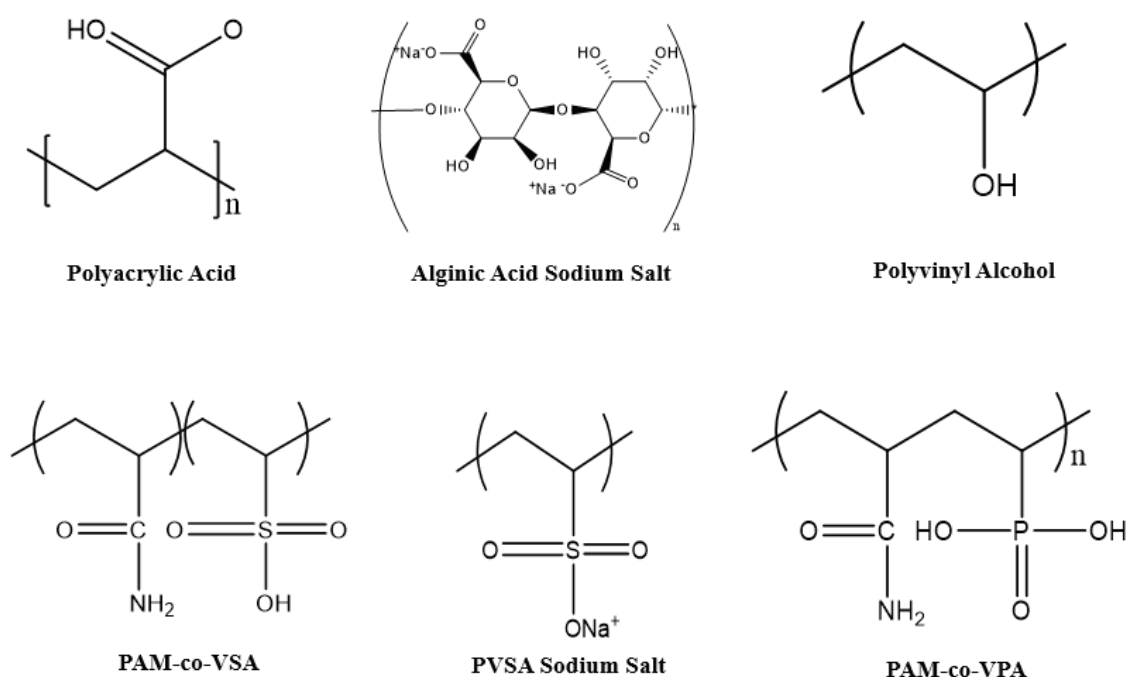


Figure 2.2. Chemical structures of polymeric antiscalants

2.5. Characterization Tools

2.5.1. X-Ray Diffraction (XRD)

XRD plays a role in determining the crystal structure by sending x-rays to the crystalline surface of the substance. Diffracted x-rays recorded and diffraction pattern shows us intense or weak reflections. We can analyze its crystalline composition, lattice parameter, space group, and many different phases according to intense or weak peak situations.³³

2.5.2. X-Ray Fluorescence (XRF)

The basic principle of XRF is the interaction of x-rays with the surface of the matter, which results in electron excitation. Then excited electrons return to their ground state, the relaxation, and emits the x-rays of the element. This method is better for analyzing the elemental composition of solid and liquid compounds but not required for inhomogeneous solid substances.³⁴

2.5.3. Fourier Transform Infrared Spectroscopy (FTIR)

FTIR method studies the transmission and absorption of chemical structures. Two different technologies are used for FTIR measurements. One of them is the KBr disk technique, which is very useful for normal characterization. Another one is ATR, which is also used for liquid samples. The basic principle of infrared is to study the chemical composition and structural bonding.³⁵

2.5.4. Inductively Coupled Plasma – Optical Emission Spectroscopy (ICP-OES)

Inductively coupled plasma optical emission spectroscopy is used to analyze the concentration of elements in liquid samples at ppb level. It is also better to analyze heavy trace metals with ICP-OES because of the low detection limit, large linear range, and multi-elemental analysis.³⁶

2.5.5. Scanning Electron Microscopy (SEM)

Scanning electron microscopy is a technique that can help us to see the specimen's surface morphology at the nanometer level. In a vacuum media (10^{-4} - 10^{-10} Torr), voltage is sending between the filament and the conductive surface. Then it causes electron emission from filament to the specimen, and surface morphology can be determined by secondary electrons.³⁷

CHAPTER 3

Results and Discussion

3.1. Structural, Morphological and Spectroscopic Analysis of Natural Deposit

3.1.1. XRD and XRF of Natural Deposits

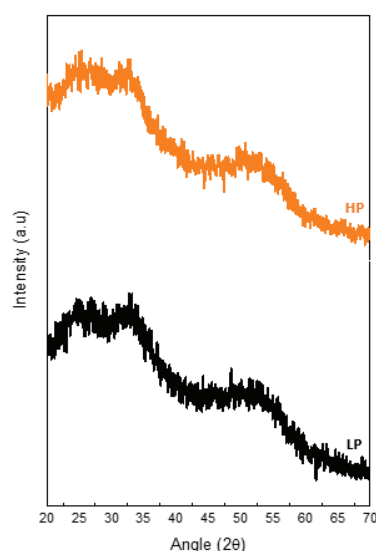


Figure 3.1. XRD results of low pressure (LP) and high pressure (HP) area samples

The deposits we collected from the preheaters were investigated with XRD and XRF. Normally, stibnite has been observed as both crystalline (dark-gray) and amorphous (orange-red). The amorphous form is known as metastibnite.²⁶ Unlike the crystalline form, we cannot determine which phases the sample contains for the amorphous (colloidal) samples. The reason may be the existence of polymeric antiscalants used for changing the crystalline structure of stibnite to amorphous. Shortly, the lattice form of Sb_2S_3 changes. Figure 3.1 shows that our samples are amorphous stibnite because no specific or intense reflections can be seen.

Table 3.1. XRF results of high and low-pressure area samples

Element	High-Pressure Area (%)	Low-Pressure Area (%)
Na	17.26	24.17
Mg	2.538	2.708
S	2.967	4.291
Sb	46.34	35.86

However, for these situations, another technique is used for the elemental analysis of deposits. XRF results demonstrate the mass (%) composition of elements in the deposit, so we can estimate the molecular formula and understand which elements are present in the deposit. Table 3.1 shows the elemental mass (%) composition of the high- and low-pressure area samples. The reason could be both areas have different temperatures. Thus, the deposition rate changes from the HP to LP areas.

3.1.2. SEM of Natural Deposits

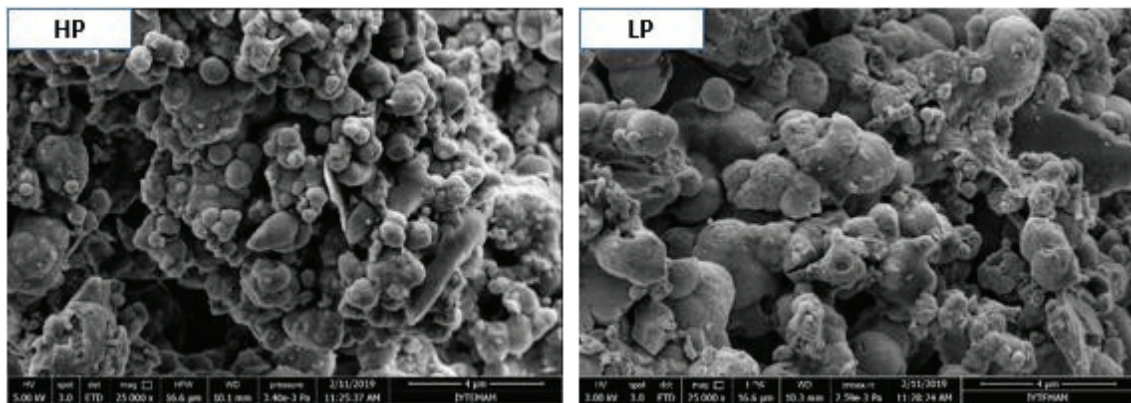


Figure 3.2. SEM images of deposits obtained from High and Low-Pressure areas ($\times 25k$).

Normally, without using any inhibitor, stibnite has been seen in black-crystalline and red-amorphous forms.¹⁰ However, using polymeric antiscalants changes its crystalline lattice form to colloidal (amorphous) particles. The reason is known as the chelating effect of the polymer. The chelating agent, which is an organic compound (ligands), binds to metal ions and blocks them from forming crystalline molecules.

Shortly, it prevents the covalent bond between Sb^{3+} and S^{2-} atoms and disrupts the crystalline structures.

Table 3.2. EDX results of the sample which were taken from a high and low-pressure area

High Pressure		Low pressure	
Element	Wt (%)	Element	Wt (%)
C	10.76	C	13.57
O	6.74	O	7.07
Na	0.57	Si	0.33
Al	0.26	Br	0.59
Si	0.44	S	21.87
S	22.06	Sb	56.57
Sb	59.17		

Table 3.2 shows EDX results of HP and LP area samples as a mass (%). The electron microscope picks an area from scanning electron images, and it starts to scan the specific area of samples. From these results, it is clear that antimony and sulfide elements are common in these areas.

3.1.3. FTIR Study

Table 3.3. Represents IR transmission bands in natural inhibitor, HP, and LP samples

Natural Inhibitor (Commercial)		HP	LP
O-H band	3002 cm^{-1}	-	-
C=O band	1717 cm^{-1}	-	-
N-O band	1561 cm^{-1}	1561 cm^{-1}	1556 cm^{-1}
S=O band (sulfonyl chloride)	1408 cm^{-1}	1393 cm^{-1}	1394 cm^{-1}
C-O (primary alcohol)	1085 cm^{-1}	-	-

A natural inhibitor is unidentified. Therefore, FTIR analysis helps us find the chemical bonds in the molecules that produce absorption or transmission spectrum. Strong O-H and C=O were seen at 3002 cm^{-1} and 1717 cm^{-1} . However, these bands were not seen in high-pressure and low-pressure area samples (HP and LP were treated with natural inhibitor). Strong N=O and S=O bands were obtained from all of the samples, but the C-O stretching band was only seen in the commercial inhibitors. These results mean that the exact structure of the molecule cannot be found according to FTIR results, but it is predictable which chemical bonds exist in the structure of the molecule.

CHAPTER 4

SATURATION INDEX

4.1. Thermodynamic Aspect of Saturation Index

Considering the many literature studies, geothermal brine compositions are monitored depending on the mineral-solution relationship in the presence of various elements. Temperature change generally causes mineral saturation. These changes may result in mineral precipitation.

For calculation of saturation index pH, Eh and temperature play an important role. According to a suitable mineral phase, the saturation index of the solution and partial pressure of gases can be calculated. Considering the chemical equilibrium, Gibbs free energy may be at a minimum in a thermodynamic system. The reaction which shows the change in Gibbs free energy at constant temperature and pressure is shown below:

$$\Delta G = \sum v_p \cdot \mu_p - \sum v_r \cdot \mu_r \quad (16)$$

where μ_r and μ_p both represent the chemical potential of reactants and products. V_p and V_r are stoichiometric coefficients. The related equation of chemical potentials shown below:

$$\mu_p = \mu_p + RT \ln A_p \quad (17)$$

$$\mu_r = \mu_r + RT \ln A_r \quad (18)$$

where R, T, A_p , and A_r corresponds to the gas constant, the absolute temperature the activity of the products and reactant species, respectively,

$$\Delta G = \sum_P V_P [\mu_p + RT \ln A_p] - \sum_r V_r [\mu_r + RT \ln A_r]$$

$$= \sum_p V_p \mu_p - \sum_r V_r \mu_r + RT \sum_p \ln(A_p^{Vp}) - RT \sum_r \ln(A_r^{Vp}) \quad (19)$$

$$\Delta G = \Delta G + RT \sum_p \ln(a_i^{Vi}) = \Delta G + RT \ln \prod (a_i^{Vi}) \quad (20)$$

where ΔG represents the Gibbs free energy, and the remaining reaction refers to reactants and products. Also, the value of V_i positive for reactants, negative for products. Also, equation 21 shows the ion activity of products.

$$Q = \prod a_i^{Vi} = \frac{a_A^{VA} \cdot a_B^{VB} \dots}{a_M^{VM} \cdot a_N^{VN} \dots} \quad (21)$$

The value of K represents the equilibrium constant. When the $\Delta G=0$ and $Q=K$, this means that the reaction is in equilibrium.

$$\begin{aligned} \Delta G &= -RT \ln K \\ \Delta G &= -RT \ln K + RT \ln Q = \frac{Q}{K} \end{aligned} \quad (22)$$

The saturation index (SI) is also expressed as the reaction between the mineral and aqueous solution

$$SI = \log \frac{Q}{K} \quad (23)$$

The ion activity product symbolized by Q explains the reaction between mineral and water, and K is constant. If the SI is equal to zero, this means the reaction is at an equilibrium point. If it is positive, the reaction is supersaturated, and when it becomes negative, the reaction solution is undersaturated.³⁸⁻⁴⁷

4.2. Saturation Index of Antimony Sulfide Scaling

Depending on the geological conditions in geothermal power plants, mineral precipitation in geothermal wells are one of the most important problems affecting the efficiency of the plant. Therefore, determining the optimum reinjection temperature using chemicals (antiscalants) is possible by obtaining mineral saturation diagrams.

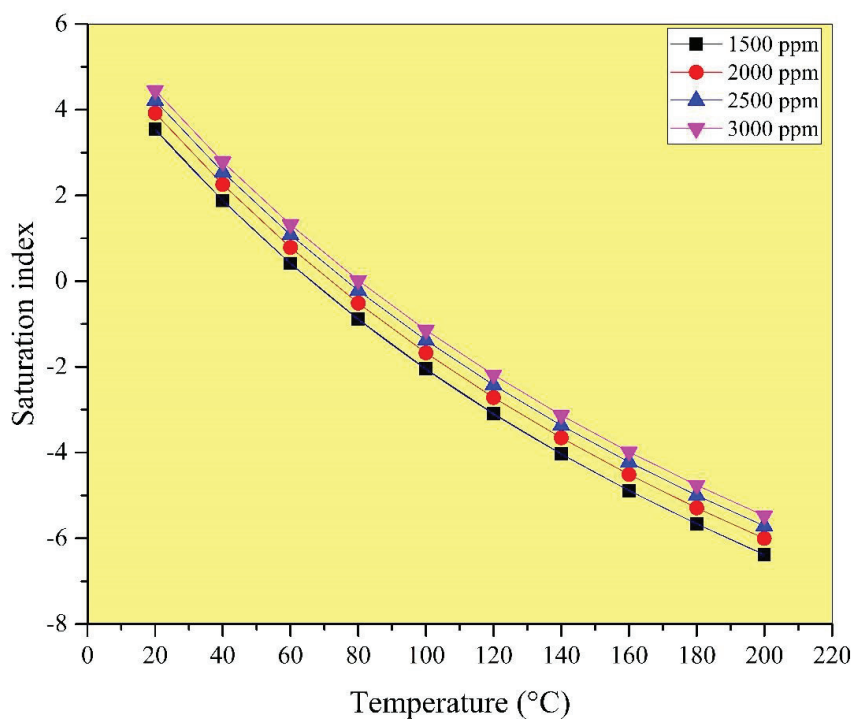


Figure 4.1. Stibnite solubility diagram at different H₂S concentrations

The saturation index graph of stibnite mineral at 1500 ppm, 2000 ppm, 2500 ppm, and 3000 ppm H₂S concentrations is given in Figure 4.1. The saturation index value of stibnite is equal to zero at approximately 90°C. This means the relevant geothermal fluid is in equilibrium with the stibnite mineral. At temperatures below 90°C, the geothermal fluid becomes saturated with the stibnite mineral, and stibnite precipitation begins. Therefore, it is appropriate to have the optimum reinjection temperature at 95°C.

CHAPTER 5

ARTIFICIAL DEPOSIT

5.1. Synthesis of Artificial Deposits

In the beginning, for synthesizing stibnite, 500 ppm, 1000 ppm, 5000 ppm, 10000 ppm (10g/L) reactions were prepared at 80°C in a two-necked balloon with a reflux system. Reaction continued for two hours. Results were analyzed with SEM and XRD techniques.

5.1.1. XRD of the Artificial Deposit

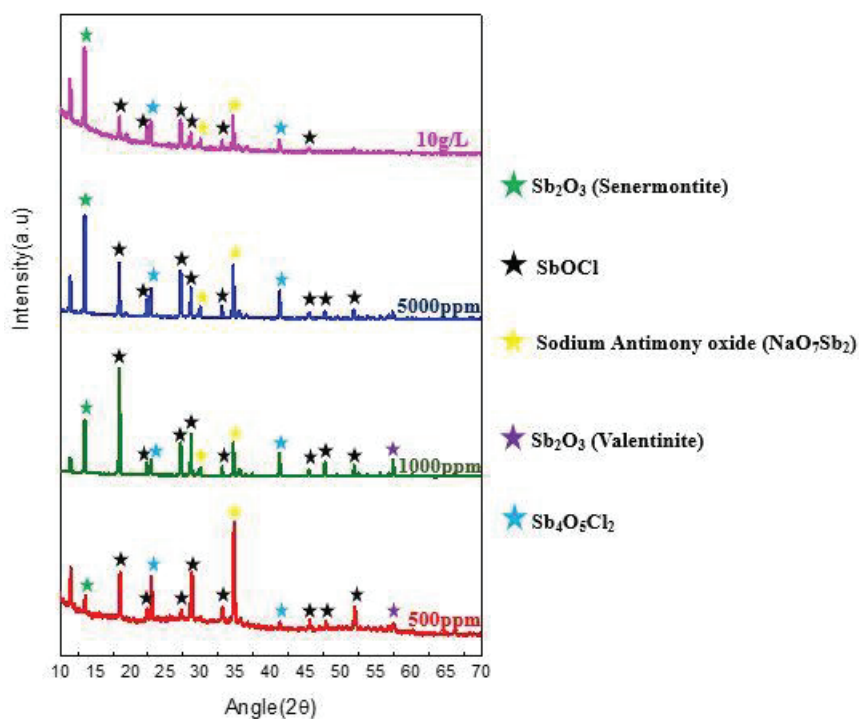


Figure 5.1. XRD patterns show from bottom to top 500ppm, 1000ppm, 5000ppm, and 10g/L reactions at 80°C.

These results showed that under 100°C (1atm), many different phases could be seen, and mostly the SbOCl phase is common. The reaction between SbCl₃ and water results in SbOCl, and hydrochloric acid released. The addition of Na₂S changes the color of the reaction from white to orange, but under 100°C, SbOCl cannot be dissolved exactly to react with S²⁻ ions to form antimony trisulfide (Sb₂S₃).³²

5.1.2. SEM of the Deposit

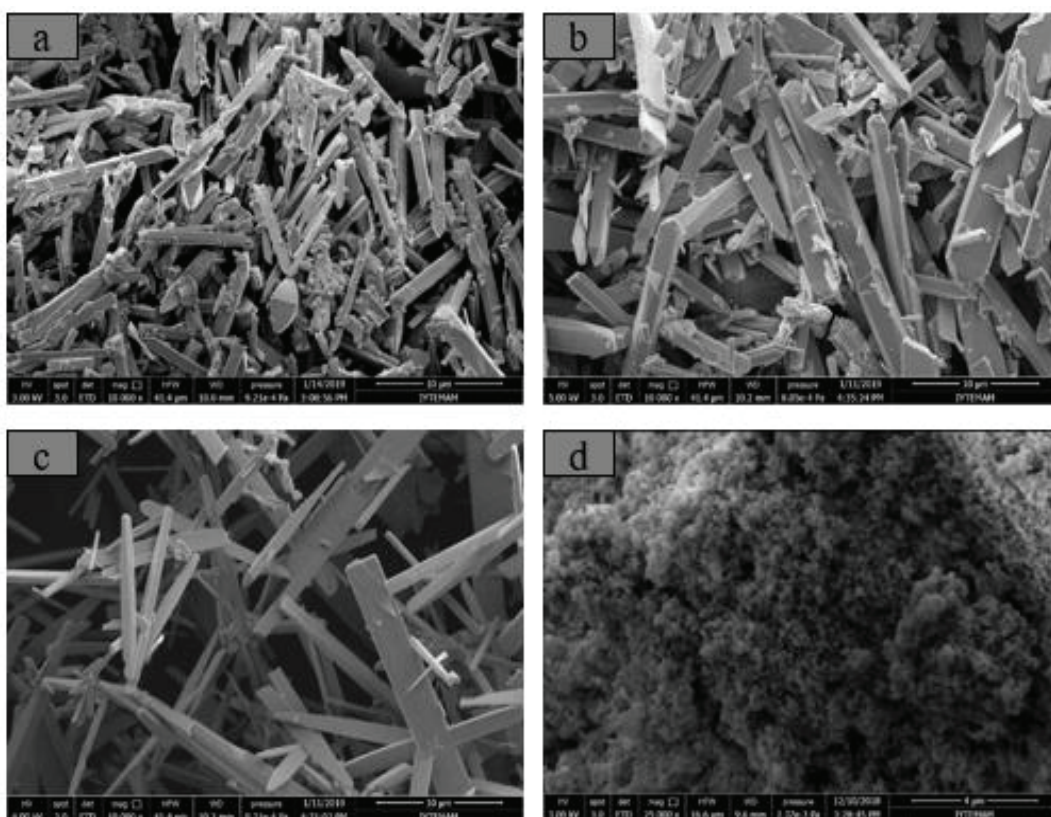


Figure 5.2. SEM images of the synthesized precipitates (a) 500 ppm ×10k. (b) 1000 ppm ×10k. (c) 5000 ppm ×10k. And (d) 10 g/L ×25k. at 80°C, 2h using reflux system.

Figure 5.2 demonstrates that the SEM images of 500 ppm and 1000 ppm reaction of SbOCl crystals are thicker than the others. The reason for that is increasing the concentration of the solution causes more thinner and needle-like crystals (5000 ppm). Moreover, when the concentration increases 20 times, the crystalline structure turns to amorphous crystals.

5.1.3. Structural and Morphological Analysis of Artificial Stibnite Deposit

The results for the reflux system showed that under 100°C SbOCl crystals have been synthesized. The reaction was carried out from the autoclave. The reason for the usage of the autoclave is to reach higher temperatures ($>100^{\circ}\text{C}$) and pressure (3 bar). Fig. 3.5 shows that 1000 ppm of 2h, 4h, 8h, 12h, and 16h stibnite synthesis. At first, the reaction continues 2h. After 2h, brown-reddish Sb_2O_3 particles were obtained. Increasing the period of time, it has been clearly seen that the Sb_2O_3 turns to Sb_2S_3 . There was no Sb_2O_3 peak seen from the 8th hour. However, the optimum synthesis timing for crystalline stibnite is determined as 12h. At 16h, it is still stibnite, but amorphous particles are also seen.

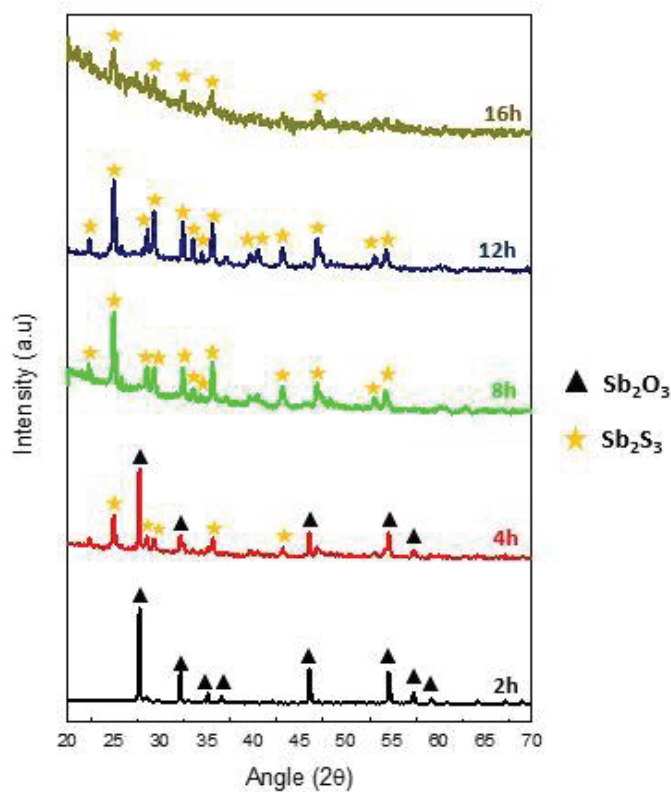


Figure 5.3. X-Ray Diffractogram of the precipitates prepared at various reaction times.

In Figure 5.4, it is seen that color visibly change during the reaction time. After 2h, it changes from reddish-brown to black, and it is stable in black-greyish at 4h, 8h, 12h, and 16h. Thus, it is understood that stibnite crystals begin to form after 2h.

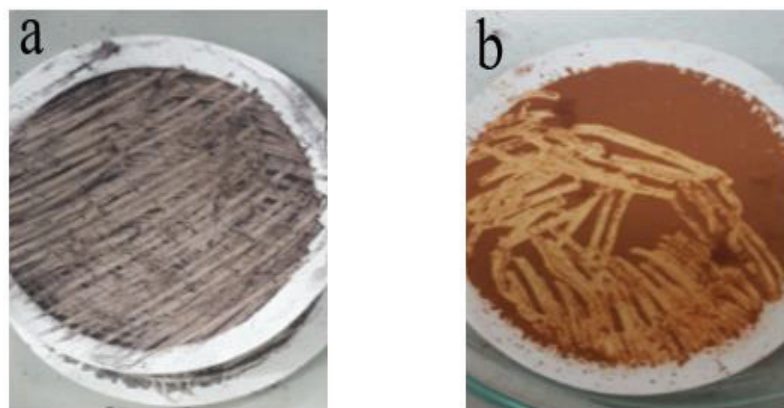


Figure 5.4. Photographs show that the color-changing a) 12h at 137°C (3 bar) black-greyish stibnite crystals, b) 2h at 137°C (3 bar) antimony trioxide reddish-brown particles.

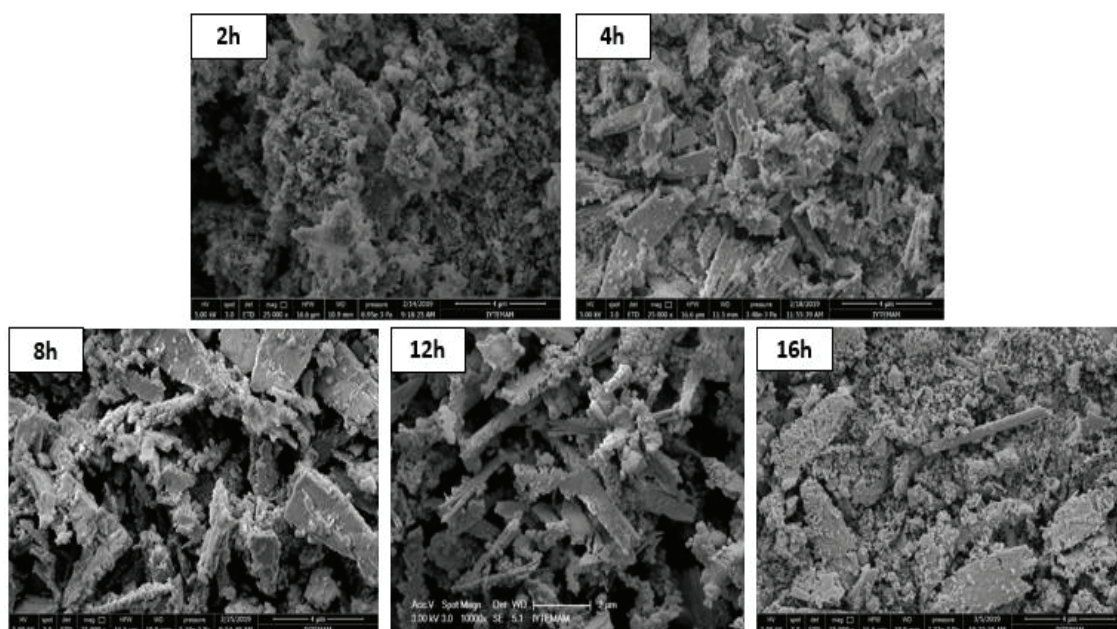


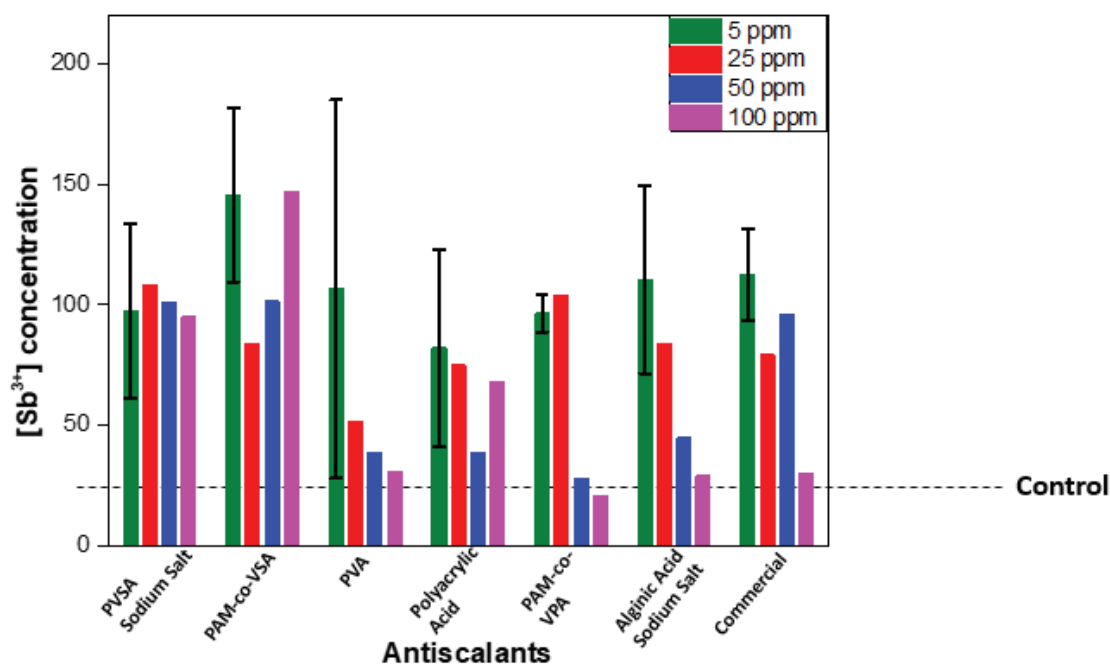
Figure 5.5. SEM images of 2h (Sb_2O_3), 4h, 8h, 12h, 16h stibnite crystals ($\times 25\text{k}$)

SEM was used to study the morphology of the artificial deposit. Figure 5.5 shows the artificial stibnite deposits, which were synthesized by autoclave at high temperature. All deposits have an orthorhombic crystal structure, and at 2h, the stibnite crystals have not formed yet. After 4h and 8h, crystals get shaped; in 12h, they became rod-like stibnite crystals. Although the orthorhombic stibnite crystals were observed in 16h reaction, colloidal particles are also commonly seen. Thus, more than 12h colloidal particles become more predominant.

5.2. Screening Tests Using Polymeric Antiscalant

There are seven water-soluble polymeric inhibitors used for the inhibition test of stibnite. From those, three of them, [P(AM-co-VSA)], [P(AM-co-VPA)], and PVSA sodium salt were synthesized in the laboratory⁵. One is commercial, and the others are polyacrylic acid, polyvinyl alcohol, and alginic acid sodium salt. For testing the inhibition performance 5, 25, 50 and 100 ppm dosages of polymeric antiscalants were added to the reaction. Again, a 1000 ppm stibnite reaction was prepared. In addition, different dosages of inhibitors were added for each reaction. The reaction continues 12h at 137°C (3 bar), and after the reaction ends, the solution was taken into the ice bath. The cooling process took 30 min; then, the solution was centrifuged for 15 min at 6000 RPM. After that, decantate and solid products separated. Decantate was acidified with 2% HNO₃ (v/v) for ICP-OES, and the solid product was put into a vacuum oven at 60°C for 12h. The solid product was analyzed with XRD and FTIR.

Normally, the inhibition efficiency of [P(AM-co-VSA)], [P(AM-co-VPA)], and PVSA was tested for metal-silicate deposition⁵. Thus, Figure 5.6 shows the change in [Sb³⁺], and [S²⁻] concentration levels in the presence of 5, 25, 50 and 100 ppm dosages of chemical inhibitors and how the metal-silicate inhibitors work in the presence of metal-sulfide deposits.



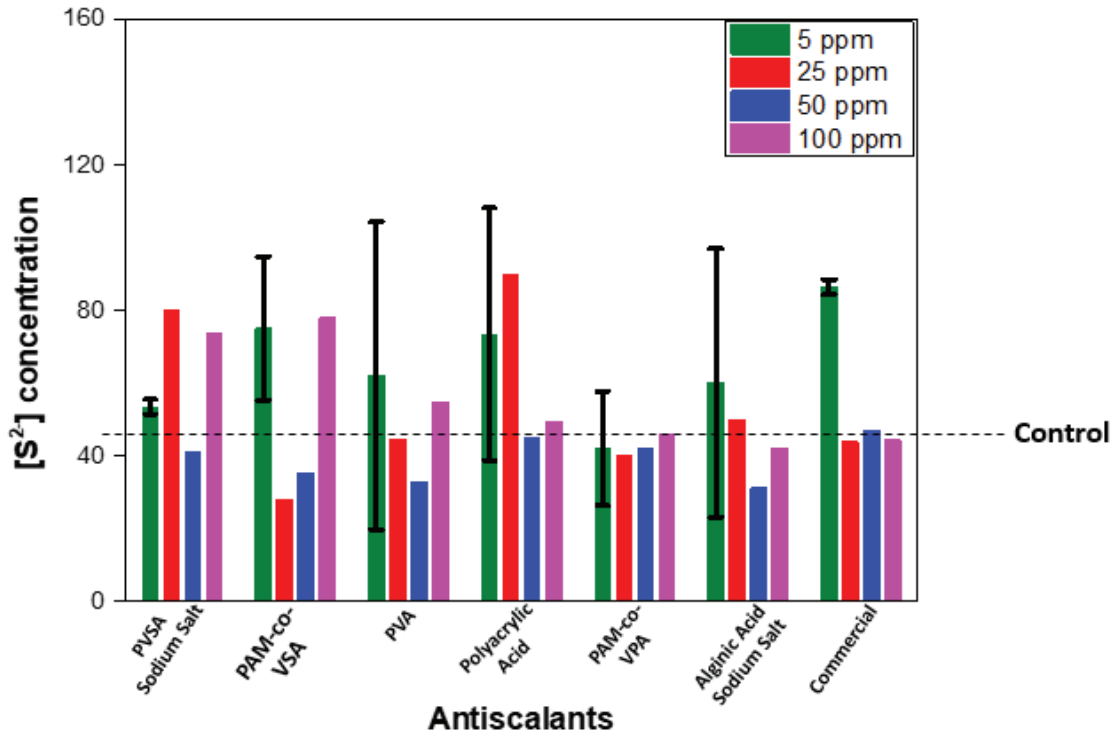


Figure 5.6. ICP-OES results show the change in $[Sb^{3+}]$, and $[S^{2-}]$ concentrations in the presence of 5, 25, 50, and 100 ppm dosage of antiscalants and the control sample refers to blank solution.

According to these results, three chemical antiscalants showed the highest increase in antimony concentration levels for each dosage. For the 5 ppm dosage of antiscalants, PAM-co-VSA, alginic acid sodium salt and commercial product show the better result for increasing the $[Sb^{3+}]$ concentration in the solution. PVSA sodium salt, PAM-co-VSA, and PAM-co-VPA were most effective for the 25 ppm dosage. PVSA sodium salt, PAM-co-VSA, and commercial gave better inhibition for the 50 ppm dosage. Considering the 100 ppm dosage, PVSA sodium salt, PAM-co-VSA, and polyacrylic acid increase the antimony concentration levels better than other chemical inhibitors. To understand this better, Table 3.4 shows the inhibition efficiency of these three inhibitors on $[Sb^{3+}]$ concentration. Percent inhibition was calculated according to this equation, where C_E , C_0 , and C_T represent Sb concentration in the presence of inhibitor, Sb concentration in the absence of inhibitor present, and the initial amount of Sb, respectively.²⁴

$$[C_E - C_0] / [C_T - C_0] \times 100\% \quad (15)$$

Table 5.1. Represents the percent inhibition efficiencies of $[Sb^{3+}]$ concentration in the presence of 5, 25, 50 and 100 ppm inhibitor dosage.

5 ppm	% Performance
PVSA Sodium Salt	38
PAM-co-VSA	57
Alginic Acid Sodium Salt	44
25 ppm	% Performance
PVSA sodium salt	32
PAM-co-VSA	23
PAM-co-VPA	31
50 ppm	% Performance
PVSA sodium salt	30
PAM-co-VSA	30
Commercial	28
100 ppm	% Performance
PVSA sodium salt	27
PAM-co-VSA	47
Polyacrylic Acid	17

From the table, considering the inhibition dosages, the addition of 5 ppm of PAM-co-VSA shows only 57% of $[Sb^{3+}]$ inhibition. Compared to Figure 5.6, the $[Sb^{3+}]$ ions in the solution are higher for chosen inhibitors, but it does not show the inhibition efficiency of $[Sb^{3+}]$ concentration. With the formula above, the initial amount of Sb in the $SbCl_3$ was calculated (C_T). After that, this value was put into the formula, and inhibition efficiency was evaluated. These results are not good for $[Sb^{3+}]$ inhibition. This is because it is, normally explained that a lower concentration of antiscalants, used between 5 ppm to 10 ppm dosages shows promising results. ^{24, 26, 27}

Hard acid soft base (HASB) interactions may exist between the ions and the ligands of the antiscalants that may govern the performance of the antiscalant. According to the HASB theory, soft acids prefers to form strong bond with soft bases, on the other hand, hard acids form strong bonds with hard bases. Sb cation seems better prevented in decantate solution compared to S^{2-} . Sb cation is soft base and it may interact with soft acid. The antiscalants we employ here have soft acid feature, which is

more polarizable. On the other hand, S^{2-} is known as moderate base so that it has less tendency to form bonds with the antiscalants. In future work we plan to enrich the list of antiscalants which have different strength of acid and base according to HASB theory such as polyethylene oxide, polyethylene imine, and their derivatives.

5.3. Structural and Morphological Analysis of Artificial Deposit After Addition of Various Polymeric Antiscalants

5.3.1. XRD Study

After the addition of 5, 25, 50, and 100 ppm dosage of inhibitors into the artificial stibnite deposit, some morphological changes were explained in Figure 5.7. The change in morphology and structure was analyzed by SEM and XRD.

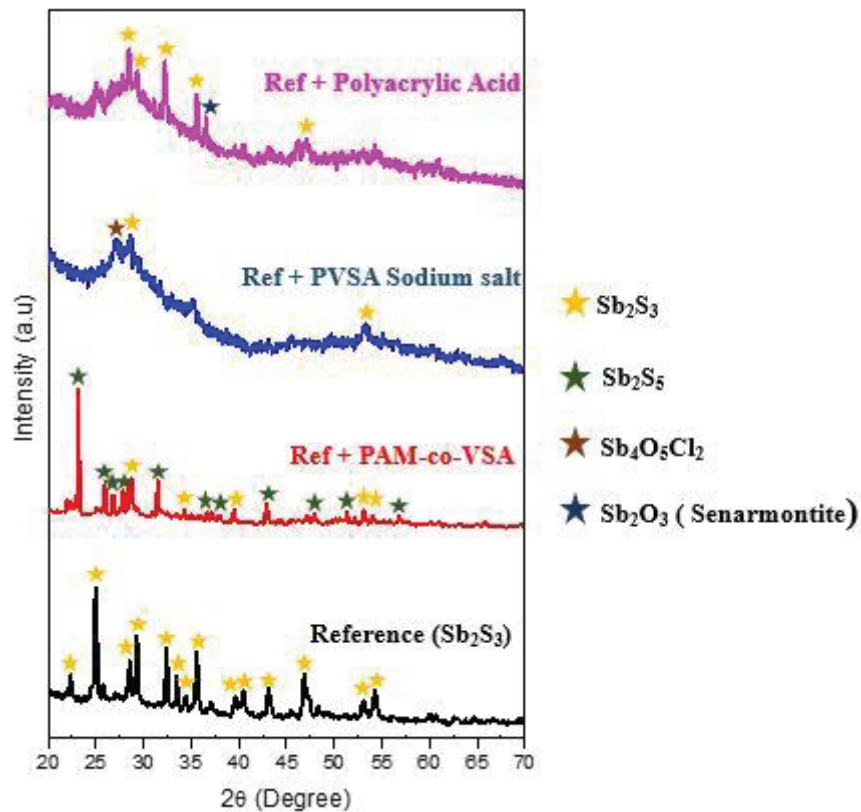


Figure 5.7. X-ray Diffractogram of inhibited powder in the presence of 100 ppm dosage of PAM-co-VSA, PVSA, and Polyacrylic Acid

The addition of 100 ppm dosage of PAM-co-VSA, PVSA sodium salt, and polyacrylic acid changes the crystallography of the reference sample. In the presence of PAM-co-VSA, there are two crystal phases apparent as Sb_2S_3 and Sb_2S_5 , respectively. When PVSA is used for inhibition, besides the orthorhombic stibnite crystal phase, antimony oxide chloride ($\text{Sb}_4\text{O}_5\text{Cl}_2$), the monoclinic crystal phase, exists. After polyacrylic acid was used, antimony trioxide (Sb_2O_3), which has an orthorhombic phase, formed.

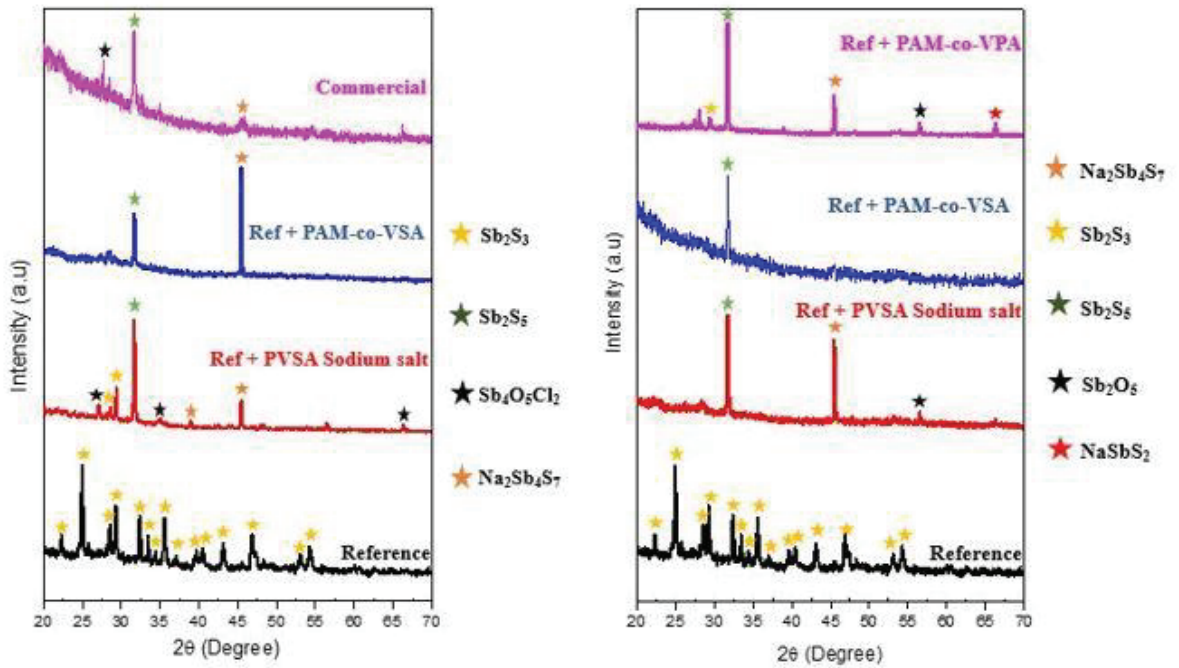
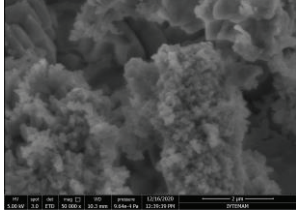
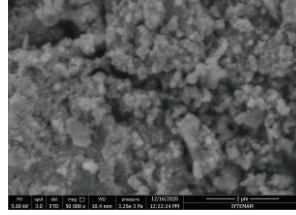
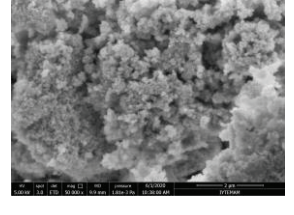
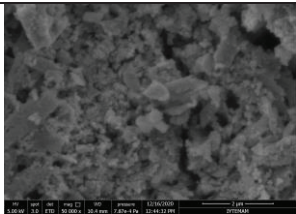
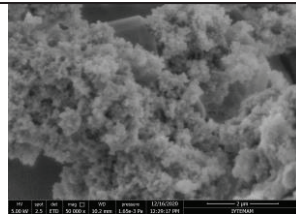
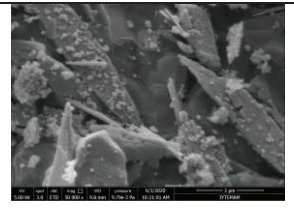
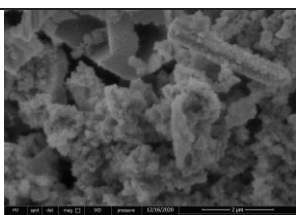
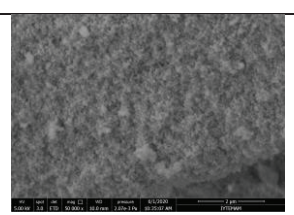
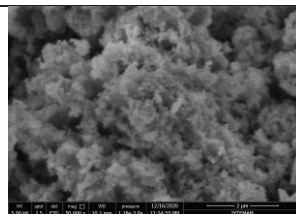


Figure 5. 8. X-ray Diffractogram of inhibited powder in the presence of 50 and 25 ppm dosage of Antiscalants

When the 50 ppm dosage of PVSA sodium salt, PAM-co-VSA, and commercial antiscalants was added to the system, the crystallography of the reference sample was changed. In the presence of three different antiscalants, the monoclinic crystal phase of antimony oxide chloride and sodium antimony sulfide exist. Besides them, the antimony pentasulfide phase was also observed. Moreover, in the presence of 25 ppm dosage of PVSA sodium salt, PAM-co-VSA, and PAM-co-VPA, different phases were analyzed. Except for the phases that can be seen at 50 ppm, the antimony pentaoxide and cubic crystal phase of sodium antimony sulfide was formed. These results show that in the presence of various antiscalant dosages, the morphology of the stibnite was changed.

5.3.2. SEM Study

	DOSAGES		
Antiscalants	25 ppm	50 ppm	100 ppm
PVSA Sodium Salt			
PAM-co-VSA			
PAM-co-VPA			
Poly[acrylic acid]			
Commercial			

Tablo 5.2. Representative SEM images of the three best antiscalants that increase the concentration of antimony in the solution at different dosages.

The addition of the 25, 50, and 100 ppm dosage of the chosen antiscalants changes the morphology of the reference scale. The reference sample, which has rod-like crystals, changed to colloidal particles for almost each antiscalant. However, the addition of 100 ppm dosage of PAM-co-VSA makes crystals bigger.

5.3.3. FTIR Study

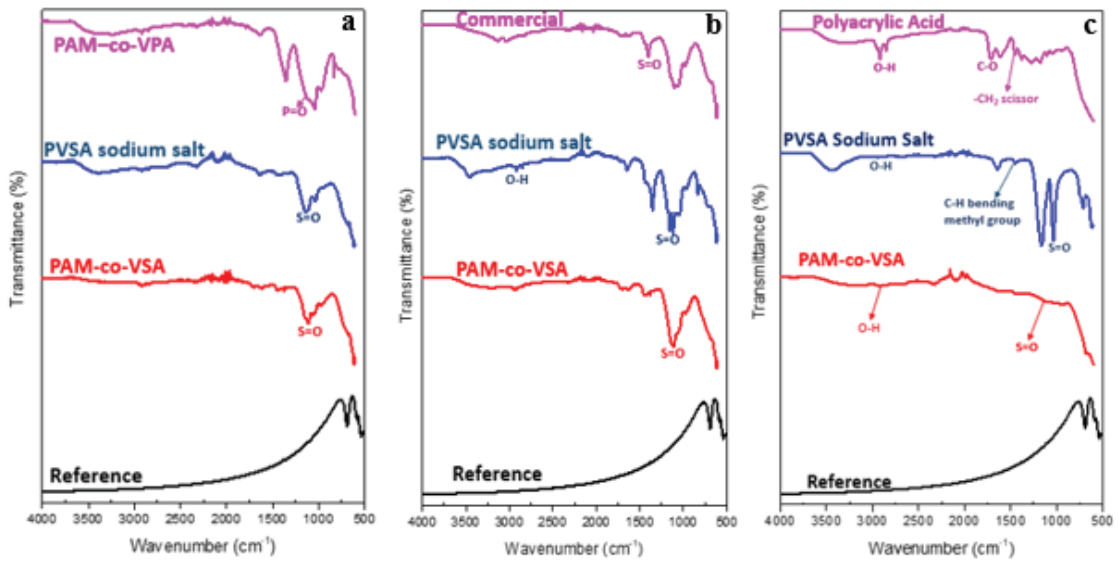


Figure 5. 9. Represents the FTIR spectrum of scale in the presence of a) 25 ppm, b) 50 ppm and c) 100 ppm dosage of antiscalants

After the inhibition process, the remaining scale was analyzed by FTIR. The reason we look at FTIR analysis is, to determine whether our scale contains polymeric antiscalant. For PAM-co-VSA and PVSA sodium salt, which contains a sulfonic acid group, was observed. Also, phosphonic acid and carboxyl groups were observed for PAM-co-VPA and Poly[acrylic acid], respectively. Considering the commercial product, the structure was not known. However, with FTIR, the functional group of commercial antiscalant was obtained clearly.

CHAPTER 6

CONCLUSION

In this thesis, the natural antimony sulfide scale was analyzed by FTIR, XRF, SEM, and XRD techniques first. After that, the artificial deposit was synthesized in an autoclave reactor at 137°C, 12h. From the x-Ray diffractogram, it is understood that pure crystalline stibnite was obtained. Also, inhibition experiments were done in the same conditions. For inhibition experiments, different dosage of antiscalants, which are PVSA sodium salt, PAM-co-VSA, PAM-co-VPA, Poly[acrylic acid], Poly[vinyl alcohol], alginic acid sodium salt, and commercial product, were used. At higher dosages, PVSA sodium salt, PAM-co-VSA, and Poly[acrylic acid] increase the antimony concentration in the solution. Although the high dosage works well in one aspect, it is not cost-efficient. Compared to higher dosages, the 5 ppm dosage of PAM-co-VSA, alginic acid sodium salt, and commercial antiscalant increases the antimony concentration in the solution well. However, when the antiscalant performances were calculated, only PAM-co-VSA shows the 57% antiscalant performance. Other antiscalants performed below 50%.

In summary, the 5 ppm dosage of PAM-co-VSA shows good antiscalant performance and it is cost-efficient. From that knowledge, it is understood that polymers with sulfonic acid groups play a more effective role in antimony inhibition in geothermal binary plants.

REFERENCES

1. Demir, M. M.; Baba, A.; Atilla, V.; Inanlı, M., Types of the scaling in hyper saline geothermal system in northwest Turkey. *Geothermics* **2014**, *50*, 1-9.
2. Wang, C.; Li, S.-p.; Li, T.-d., Calcium carbonate inhibition by a phosphonate-terminated poly (maleic-co-sulfonate) polymeric inhibitor. *Desalination* **2009**, *249* (1), 1-4.
3. Gill, J. S., Scale control in geothermal brines—new inhibitors for calcium carbonate and silica control. *Geotherm Res Counc Trans* **2008**, *32*, 207-211.
4. Pátzay, G.; Kármán, F. H.; Póta, G., Preliminary investigations of scaling and corrosion in high enthalpy geothermal wells in Hungary. *Geothermics* **2003**, *32* (4-6), 627-638.
5. Topçu, G. k.; Çelik, A.; Baba, A.; Demir, M. M., Design of polymeric antiscalants based on functional vinyl monomers for (Fe, Mg) silicates. *Energy & Fuels* **2017**, *31* (8), 8489-8496.
6. Demadis, K. D.; Mavredaki, E.; Somara, M., Additive-driven dissolution enhancement of colloidal silica. 1. Basic principles and relevance to water treatment. *Industrial & engineering chemistry research* **2011**, *50* (22), 12587-12595.
7. Demadis, K. D.; Mavredaki, E.; Somara, M., Additive-driven dissolution enhancement of colloidal silica. 2. Environmentally friendly additives and natural products. *Industrial & engineering chemistry research* **2011**, *50* (24), 13866-13876.
8. Demadis, K. D.; Somara, M.; Mavredaki, E., Additive-driven dissolution enhancement of colloidal silica. 3. Fluorine-containing additives. *Industrial & engineering chemistry research* **2012**, *51* (7), 2952-2962.
9. Honegger, J.; Czernichowski-Lauriol, I.; Criaud, A.; Menjoz, A.; Sainson, S.; Guezennec, J., Detailed study of sulfide scaling at la courneuve nord, a geothermal exploitation of the Paris Basin, France. *Geothermics* **1989**, *18* (1-2), 137-144.
10. Kaypakoglu, B.; Aksoy, N.; Serpen, U.; Sisman, M. In *Stibnite scaling in a binary power plant in Turkey*, Proceedings, 2015.
11. Majeed, N. S., Polymeric materials for scale inhibition in cooling water systems. *Tikrit Journal of Engineering Sciences* **2011**, *18* (2), 1-11.
12. Ölçenoğlu, K., Scaling in the reservoir in Kizildere geothermal field, Turkey. *Geothermics* **1986**, *15* (5-6), 731-734.

13. Fu, C. E.; Zhou, Y. M.; Liu, G. Q. In *Novel non-phosphorous antiscalants for inhibition of calcium phosphate and calcium sulfate precipitation*, Advanced Materials Research, Trans Tech Publ: 2011; pp 117-123.
14. Zarrouk, S. J.; Woodhurst, B. C.; Morris, C., Silica scaling in geothermal heat exchangers and its impact on pressure drop and performance: Wairakei binary plant, New Zealand. *Geothermics* **2014**, *51*, 445-459.
15. Gallup, D. L. In *pH modification scale control technology*, Proceedings International Workshop on Mineral Scaling, Manila, Philippines, 2011; pp 39-46.
16. Spinhaki, A.; Petratos, G.; Matheis, J.; Hater, W.; Demadis, K. D., The precipitation of “magnesium silicate” under geothermal stresses. Formation and characterization. *Geothermics* **2018**, *74*, 172-180.
17. Demadis, K. D.; Ketsetzi, A.; Sarigiannidou, E.-M., Catalytic effect of magnesium ions on silicic acid polycondensation and inhibition strategies based on chelation. *Industrial & engineering chemistry research* **2012**, *51* (26), 9032-9040.
18. Çelik, A.; Topçu, G.; Baba, A.; Akdogan, Y.; Şentürk, U.; Demir, M. M., Experimental modeling of silicate-based geothermal deposits. *Geothermics* **2017**, *69*, 65-73.
19. Topcu, G.; Çelik, A.; Kandemir, A.; Baba, A.; Sahin, H.; Demir, M. M., Increasing solubility of metal silicates by mixed polymeric antiscalants. *Geothermics* **2019**, *77*, 106-114.
20. Neofotistou, E.; Demadis, K. D., Silica scale inhibition by polyaminoamide STARBURST® dendrimers. *Colloids and Surfaces A: Physicochemical and Engineering Aspects* **2004**, *242* (1-3), 213-216.
21. Demadis, K. D.; Neofotistou, E.; Mavredaki, E.; Tsiknakis, M.; Sarigiannidou, E.-M.; Katarachia, S. D., Inorganic foulants in membrane systems: chemical control strategies and the contribution of “green chemistry”. *Desalination* **2005**, *179* (1-3), 281-295.
22. Wilson, N.; Webster-Brown, J.; Brown, K., Controls on stibnite precipitation at two New Zealand geothermal power stations. *Geothermics* **2007**, *36* (4), 330-347.
23. Brown, K. In *Antimony and arsenic sulfide scaling in geothermal binary plants*, International Workshop on mineral scaling in geothermal environments, Philippines, 2011; pp 103-106.
24. Gill, J. S.; Muller, L.; Rodman, D. In *Inhibition of Antimony Sulfide (Stibnite) Scale in Geothermal Fields*, Proceedings annual Geothermal Resources Council meeting, 2013.
25. Çiftçi, C.; Karaburun, E.; Tonkul, S.; Baba, A.; Demir, M. M.; Yeşilnacar, M. İ., Testing the Performance of Various Polymeric Antiscalants for Mitigation of Sb-

Rich Precipitates Mimicking Stibnite-Based Geothermal Deposits. *Geofluids* **2020**, 2020.

26. Muller, L.; Gill, J. S.; Rodman, D.; Brown, K.; Robinson, R. In *Control of Metal Sulfide Deposits in Geothermal Binary Plants*, Proceeding World geothermal Congress, Melbourne, Australia, 2015.
27. Muller, L.; Gill, J. S.; Rodman, D.; Brown, K.; Robinson, R., Control and Online Removal of Metal Sulfide Deposits.
28. Ubaldini, S.; Veglio, F.; Fornari, P.; Abbruzzese, C., Process flow-sheet for gold and antimony recovery from stibnite. *Hydrometallurgy* **2000**, 57 (3), 187-199.
29. SMINČÁKOVÁ, E.; KOMOROVÁ, L., Leaching of stibnite in NaOH solutions. *reactions* **2008**, 1 (9), 10.
30. Sminčáková, E.; Raschman, P., Leaching of stibnite by mixed Na₂S and NaOH solutions. *ACTA TECHNICA CORVINIENSIS–Bulletin of Engineering* **2012**, 5, 35-37.
31. Raschman, P.; Sminčáková, E., Kinetics of leaching of stibnite by mixed Na₂S and NaOH solutions. *Hydrometallurgy* **2012**, 113, 60-66.
32. Li, C.; Yang, X.; Liu, Y.; Zhao, Z.; Qian, Y., Growth of crystalline Sb₂S₃ nanorods by hydrothermal method. *Journal of Crystal Growth* **2003**, 255 (3-4), 342-347.
33. Epp, J., X-ray diffraction (XRD) techniques for materials characterization. In *Materials characterization using nondestructive evaluation (NDE) methods*, Elsevier: 2016; pp 81-124.
34. Gupta, A. K., Total Reflection X-Ray Fluorescence Spectroscopy Working Principles. *Int. J. Core Eng. Manage* **2014**, 1 (5).
35. Madejová, J., FTIR techniques in clay mineral studies. *Vibrational spectroscopy* **2003**, 31 (1), 1-10.
36. Suleiman, J. S.; Hu, B.; Huang, C.; Zhang, N., Determination of Cd, Co, Ni and Pb in biological samples by microcolumn packed with black stone (Pierre noire) online coupled with ICP-OES. *Journal of hazardous materials* **2008**, 157 (2-3), 410-417.
37. Russell, P.; Batchelor, D.; Thornton, J., SEM and AFM: complementary techniques for high resolution surface investigations. *Veeco Metrology Group* **2001**.
38. Arnórsson, S. In *The quartz-and Na/K geothermometers: II. Results and application for monitoring studies*, Proceedings of the World Geothermal Congress: Kyushu-Tohoku, Japan, 2000; pp 935-940.
39. Arnórsson, S.; Gunnlaugsson, E.; Svavarsson, H., The chemistry of geothermal waters in Iceland. II. Mineral equilibria and independent variables controlling water compositions. *Geochimica et Cosmochimica Acta* **1983**, 47 (3), 547-566.

40. Baba, A.; Şaroğlu, F.; Akkuş, I.; Özel, N.; Yeşilnacar, M. İ.; Nalbantçılar, M. T.; Demir, M. M.; Gökçen, G.; Arslan, Ş.; Dursun, N., Geological and hydrogeochemical properties of geothermal systems in the southeastern region of Turkey. *Geothermics* **2019**, *78*, 255-271.
41. Giggenbach, W. F., Geothermal solute equilibria. derivation of Na-K-Mg-Ca geothermometers. *Geochimica et cosmochimica acta* **1988**, *52* (12), 2749-2765.
42. Gunnarsson, I.; Arnórsson, S., Amorphous silica solubility and the thermodynamic properties of H₄SiO₄ in the range of 0 to 350 C at Psat. *Geochimica et Cosmochimica Acta* **2000**, *64* (13), 2295-2307.
43. Gudmundsson, B. T.; Arnórsson, S., Secondary mineral–fluid equilibria in the Krafla and Námafjall geothermal systems, Iceland. *Applied geochemistry* **2005**, *20* (9), 1607-1625.
44. Stefánsson, A.; Arnórsson, S.; Gunnarsson, I.; Kaasalainen, H.; Gunnlaugsson, E., The geochemistry and sequestration of H₂S into the geothermal system at Hellisheidi, Iceland. *Journal of Volcanology and Geothermal Research* **2011**, *202* (3-4), 179-188.
45. Tarcan, G., *Aquifer chemistry and mineral saturation in selected high temperature geothermal areas*. United Nations University: 2001.
46. Tole, M. P.; Ármannsson, H.; Zhong-He, P.; Arnórsson, S., Fluid/mineral equilibrium calculations for geothermal fluids and chemical geothermometry. *Geothermics* **1993**, *22* (1), 17-37.
47. Plummer, L. N.; Parkhurst, D. L.; Thorstenson, D. C., Development of reaction models for ground-water systems. *Geochimica et cosmochimica Acta* **1983**, *47* (4), 665-685.